Zhu Lingxin (Orcid ID: 0000-0002-6762-7882)
Kerk Samuel, A. (Orcid ID: 0000-0001-9786-2245)
Stemmler Marc, P. (Orcid ID: 0000-0002-7866-3686)
Brabletz Simone (Orcid ID: 0000-0003-0936-1526)
Brabletz Thomas (Orcid ID: 0000-0003-2983-9048)
Weiss Stephen, J. (Orcid ID: 0000-0002-1864-6075)

Title: A Zeb1/MtCK1 Metabolic Axis Controls Osteoclast Activation and Skeletal Remodeling

Running title: Zeb1/MtCK1 Metabolic Axis Controls Bone Resorption

Authors: Lingxin Zhu[1,2,3]*, Yi Tang[2,3], Xiao-Yan Li[2,3], Samuel A. Kerk[4,5,6], Costas A. Lyssiotis[4,6,11], Wenqing Feng[3], Xiaoyue Sun[1], Geoffrey E. Hespe[2,3,7], Zijun Wang[1], Marc P. Stemmler[9], Simone Brabletz[9], Thomas Brabletz[9], Evan T. Keller[10], Jun Ma[2,3], Jung-Sun Cho[2,3], Jingwen Yang[1,8], and Stephen J Weiss[2,3,12]*

Affiliations:

[1]The State Key Laboratory Breeding Base of Basic Science of Stomatology (Hubei-MOST) & Key Laboratory of Oral Biomedicine Ministry of Education, School & Hospital of Stomatology, Wuhan University, Wuhan 430079, China.

[2]Division of Genetic Medicine, Department of Internal Medicine, University of Michigan, Ann Arbor, MI 48109, USA.

[3]Life Sciences Institute, University of Michigan, Ann Arbor, MI 48109, USA.

[4]Division of Gastroenterology, Department of Internal Medicine, University of Michigan, Ann Arbor, MI 48109, USA.

[5]Doctoral Program in Cancer Biology, University of Michigan, Ann Arbor, MI 48109, USA.

[6]Department of Molecular and Integrative Physiology, University of Michigan, Ann Arbor, MI 48109, USA.

[7]Department of Surgery, Section of Plastic Surgery, University of Michigan, Ann Arbor, MI 48109, USA.

[8]School of Dentistry, University of Michigan, Ann Arbor, MI 48109, USA

[9]Department of Experimental Medicine 1, Nikolaus-Fiebiger Center for Molecular Medicine, FAU University Erlangen-Nürnberg, Glückstr. 6, 91054 Erlangen, Germany.

[10]Department of Pathology, Department of Urology and the Institute of Gerontology, University of Michigan, Ann Arbor, MI 48109, USA.

[11]Rogel Cancer Center, University of Michigan, Ann Arbor, MI 48109, USA.

***Corresponding Authors:**

E-mail: lingxin.zhu@whu.edu.cn (L.Z.); sjweiss@umich.edu (S.J.W.)

Author list footnotes:

[12]Lead Contact: sjweiss@umich.edu (S.J.W.)

This is the author manuscript accepted for publication and has undergone full peer review but has not been through the copyediting, typesetting, pagination and proofreading process, which may lead to differences between this version and the Version of Record. Please cite this article as doi: 10.15252/embj.2022111148

Character count:

Abstract: 175 words

Main text: 11146 words

Abstract

Osteoclasts are bone-resorbing polykaryons responsible for skeletal remodeling during health and disease. Coincident with their differentiation from myeloid precursors, osteoclasts undergo extensive transcriptional and metabolic reprogramming in order to acquire the cellular machinery necessary to demineralize bone and digest its interwoven extracellular matrix. While attempting to identify new regulatory molecules critical to bone resorption, we discovered that murine and human osteoclast differentiation is accompanied by the expression of Zeb1, a zinc-finger transcriptional repressor whose role in normal development is most frequently linked to the control of epithelial-mesenchymal programs. However, following targeting, we find that Zeb1 serves as an unexpected regulator of osteoclast energy metabolism. In vivo, Zeb1-null osteoclasts assume a hyperactivated state, markedly decreasing bone density due to excessive resorptive activity. Mechanistically, Zeb1 acts in a rheostat-like fashion to modulate murine and human osteoclast activity by transcriptionally repressing an ATP-buffering enzyme, mitochondrial creatine kinase 1 (MtCK1), thereby controlling the phosphocreatine energy shuttle and mitochondrial respiration. Together, these studies identify a novel Zeb1/MtCK1 axis that exerts metabolic control over bone resorption in vitro and in vivo.

Keywords:

Zeb1; Osteoclast; Mitochondrial creatine kinase; Bone resorption; Skeletal remodeling

Introduction

As a metabolically dynamic tissue, bone is continuously remodeled by coordinated phases of active resorption and formation (Boyle *et al*, 2003; Compston *et al*, 2019; Takayanagi, 2007; Teitelbaum & Ross, 2003; Zaidi, 2007). An imbalance of skeletal remodeling arising as a consequence of increased osteoclast-mediated bone resorption leads to bone-wasting states in diseases ranging from osteoporosis and rheumatoid arthritis to periodontitis and bone metastasis (Boyle *et al.*, 2003; Compston *et al.*, 2019; Takayanagi, 2007; Teitelbaum & Ross, 2003; Zaidi, 2007). Osteoclasts, giant multinucleated cells that are specialized in their ability to resorb bone, are derived from both embryonic and hematopoietic stem cell precursors of erythromyeloid and myeloid lineages (Boyle *et al.*, 2003; Jacome-Galarza *et al*, 2019; Takayanagi, 2007; Teitelbaum & Ross, 2003; Yahara *et al*, 2020). In response to the cytokines, receptor activator of NF-kB ligand (RANKL) and macrophage colony-stimulating factor (M-CSF), monocyte precursors differentiate into pre-osteoclasts that ultimately fuse to form mitochondria-rich polykaryons (Boyle *et al.*, 2003; Jacome-Galarza *et al.*, 2019; Takayanagi, 2007; Teitelbaum & Ross, 2003; Yahara *et al.*, 2020). Upon attachment to bone, osteoclasts polarize and undergo extensive morphologic changes to form an actin ring that surrounds the ruffled border, a differentiated region of the plasma membrane that secretes protons, chloride ions and various collagenolytic enzymes into the resorption lacunae (Blangy *et al*, 2020; Boyle *et al.*, 2003; Takayanagi, 2007; Teitelbaum & Ross, 2003; Zhu *et al*, 2020). To support this activity, osteoclasts display marked increases in mitochondrial content, biomass and respiration as well as accelerated glycolytic metabolism (Arnett & Orriss, 2018; Indo *et al*, 2013; Li *et al*, 2020). As such, the transition of mononucleated myeloid precursors devoid of bone-resorbing activity to mature osteoclasts requires extensive transcriptional and metabolic reprogramming (Bae *et al*, 2017; Izawa *et al*, 2015; Murata *et al*, 2017; Nishikawa *et al*, 2015; Zeng *et al*, 2015). Nevertheless, the identity and mechanisms by which osteoclast-associated transcription factors are linked to bioenergetic modules critical to bone resorption are largely uncharacterized.

While curating transcription factors upregulated specifically during bone marrow-derived macrophage-to-osteoclast transition *in vitro*, we noted that osteoclasts unexpectedly express zinc-finger E-box binding homeobox 1, i.e., *Zeb1* (also known as *δEF1*, *Zfhx1a*, *Tcf8* or *AREB6*), a transcriptional repressor most frequently associated with developmental programs linked to epithelial-mesenchymal transitions (Francou & Anderson, 2020; Nieto *et al*, 2016; Stemmler *et al*, 2019; Vandewalle *et al*, 2009). As Zeb1 transcripts and protein expression were confirmed in

both mouse and human osteoclasts, we set out to define its potential role(s) in regulating osteoclastogenesis, bone resorption and skeletal remodeling. *In vivo*, while *Zeb1* conditional knockout mice generate normal osteoclasts in terms of number and size, bone density is markedly reduced with knockout osteoclasts displaying a hyperactive bone-resorptive phenotype. Mechanistically, we identify the ATP-buffering, mitochondrial creatine kinase 1 (MtCK1), as a previously unsuspected Zeb1 target that modulates mitochondrial phosphocreatine energy metabolism critical to mouse and human osteoclast bone resorption. Taken together, these finding identify a new Zeb1/MtCK1 metabolic axis that controls osteoclast functions central to skeletal remodeling.

Results

Osteoclasts selectively upregulate *Zeb1 in vitro* and *in vivo*

In the presence of M-CSF and RANKL, mouse bone marrow-derived macrophages (BMDMs) differentiate into multinucleated, tartrate-resistant acid phosphatase-positive (TRAP$^+$) osteoclasts within a 4-5 d culture period (Tang *et al*, 2009; Zhu *et al.*, 2020; Zou *et al*, 2016). In an effort to identify new transcription factors (TFs) expression critical to osteoclast formation or function, mouse BMDMs and osteoclasts were harvested for transcriptional profiling. As expected, gene ontology analysis identified an enrichment in DNA-binding TF activity (Fig 1A). However, among the top 20 of the most highly expressed TFs, including many of those previously linked to osteoclast differentiation (Fig 1B) (Kurotaki *et al*, 2020; Tsukasaki *et al*, 2020), we noted the unexpected expression of Zeb1 alone among the family of EMT-associated transcriptional repressors (Fig 1B). The upregulation of *Zeb1* expression was confirmed by real-time PCR and coincides with that of other well-known osteoclast maturation makers, including *Acp5* and *Ctsk* (Fig 1C). Similarly, at the protein level, Zeb1 content increases as BMDMs are induced to form osteoclasts (Fig 1D; Appendix Fig S1A). Further, using Zeb1-specific antibodies, Zeb1 was found to be extensively localized in the nucleus of cultured osteoclasts (Fig 1E). Extending these data into the *in vivo* setting, osteoclasts adherent to the bone surface display nuclear Zeb1 along with TRAP immuno-reactivity, confirming the specific expression of Zeb1 in skeletal tissues (Fig 1F). Unsupervised clustering of single cell RNA-seq analysis of deposited public dataset of E14.5 whole mouse embryos (Yahara *et al.*, 2020) assigned the cells into distinct 19 subpopulations using known marker genes (Fig EV1A) with *Zeb1* largely confined to *Dcstamp*$^+$*Ocstamp*$^+$*Atp6v0d2*$^+$*Ctsk*$^+$ osteoclast-specific as well as a *Pecam1*$^+$*Cdh5*$^+$ endothelial-specific populations (Fig EV1B; Data ref: Yahara *et al.*, 2020).

While mouse and human monocyte-derived populations share a number of functional characteristics, important distinctions also exist (Ginhoux & Jung, 2014). To assess the relevance of the mouse osteoclast Zeb1 expression to human cells, primary human CD14$^+$ monocytes were induced into macrophages prior to undergoing osteoclast differentiation upon addition of M-CSF and RANKL (Raynaud-Messina *et al*, 2018; Zhu *et al.*, 2020). Under these conditions, TRAP$^+$ multinucleated cells are generated that likewise co-express ZEB1 and CTSK at both the mRNA and protein levels (Fig EV1C-E; Appendix Fig S1B).

Zeb1 conditional knockout mice exhibit an osteopenic phenotype *in vivo*

Having identified Zeb1 expression in osteoclasts, we sought to define its role *in vivo* by generating a myeloid-specific Zeb1 conditional knockout mouse model by crossing *Zeb1*$^{f/f}$ mice with *Csf1r-Cre* mice (*Csf1r-Cre/Zeb1*$^{f/f}$; hereafter referred to as *Zeb1*$^{\Delta M/\Delta M}$; Fig EV2A), wherein Cre is expressed in myeloid progenitors, including the osteoclast-derived lineage (Compston *et al.*, 2019). We then assessed bone morphometry in 3-month-old wild-type and *Zeb1*$^{\Delta M/\Delta M}$ mice. In marked contrast to the normal bone observed in the wild-type littermates, *Zeb1* targeting elicited a marked osteoporosis-like effect with reduced trabeculation of distal bone marrow spaces in both male and female *Zeb1*$^{\Delta M/\Delta M}$ mice, resulting in a remarkable 50% drop in bone mass (Fig 2A-C; Fig EV2B). Nano computed tomography (nanoCT) scans of the distal femurs of *Zeb1*$^{\Delta M/\Delta M}$ male and female mice highlighted the striking decreases in bone volume/tissue volume, number of trabeculae and trabecular thickness in tandem with increased trabecular separation (Fig 2A-C; Fig EV2B). *Zeb1* deficiency also triggers a modest, but statistically significant, decrease in cortical bone thickness (Fig EV2C). Similar changes in cancellous bone are also observed in the lumbar vertebrae of *Zeb1*$^{\Delta M/\Delta M}$ male mice (Fig EV2D and E). Complementing these findings, serum CTX-I, a marker of bone type I collagen degradation (Srivastava *et al*, 2000)**,** increased by ~50% in the *Zeb1*$^{\Delta M/\Delta M}$ mice (Fig 2D), underlining the increase in bone-resorbing activity.

Despite the increase in bone remodeling activity, osteoclast numbers as assessed by TRAP staining the distal femur are slightly decreased in *Zeb1*$^{\Delta M/\Delta M}$ mice relative to wild-type, while the surface area of bone erosions is increased (Fig 2C and D). Higher-magnification images of Goldner's trichrome staining in the distal femur indicate that *Zeb1*$^{\Delta M/\Delta M}$ mice display enlarged gaps between osteoclasts and trabecular bone (i.e., Howship's lacunae; arrow) as a consequence of increased bone resorption (Fig 2E) (Everts *et al*, 2002). Alteration in osteoclast function can also affect osteoblast activity (Sims & Martin, 2020), but bone formation as assessed by serum osteocalcin (OCN), mineral apposition rate (MAR) or bone formation rate (BFR) did not reveal significant differences between *Zeb1*$^{\Delta M/\Delta M}$ mice and control mice (Fig 2D-F), confirming that reduced bone resorption, rather than changes in bone formation, are responsible for the osteoporosis-like phenotype. Together, these results support a model wherein osteoclast Zeb1 plays an important role orchestrating physiological bone remodeling and bone resorption *in vivo*.

Zeb1-knockout osteoclasts display enhanced bone-resorbing activity *in vitro*

To determine the role of Zeb1 targeting on osteoclast differentiation and function *in vitro,* we isolated BMDMs from *Zeb1*$^{\Delta M/\Delta M}$ mice and generated osteoclasts for functional assessment. Following *Zeb1* deletion, neither the number of CD11b^{+} osteoclast precursor cells nor the proliferative activities of BMDMs are affected (Appendix Fig S1C and D), supporting the conclusion that *Zeb1*$^{\Delta M/\Delta M}$ mice maintain a normal pool of osteoclast precursor cells. The apoptotic ratio of *Zeb1*$^{\Delta M/\Delta M}$ osteoclasts also remains unaltered either under resting conditions or following starvation (Appendix Fig S1E). Upon osteoclastogenic induction, *Zeb1*$^{\Delta M/\Delta M}$ macrophages undergo osteoclastogenesis comparably to controls as assessed by TRAP staining and TRAP^{+} multinucleated cell (MNC) number (Fig 3A). Likewise, gene expression levels of a series of osteoclast markers, including *Acp5, Nfatc1, c-fos, Dcstamp, Oscar, Itgb3, Atp6v0d2, Src,* and *Ctsk* are indistinguishable between wild-type and *Zeb1*-deficient cells as are protein expression of the osteoclast differentiation- and maturation-related markers, nuclear factor of activated T cells 1 (NFATc1), c-Fos, c-Src, β3 integrin, Mmp9, Mmp14, and Ctsk (Appendix Fig S1F; Fig 3B; Appendix Fig S2A). We further confirmed that the transcript level of *Zeb2* is not regulated in a compensatory fashion (Appendix Fig S1F) (Postigo & Dean, 2000). Given that the myeloid-specific depletion of *Zeb1* does not affect the osteoclastogenic differentiation program *in vitro*, we next assessed their bone resorptive activity *in vitro*.

In marked contrast to control osteoclasts, *Zeb1*$^{\Delta M/\Delta M}$ cells display significant increases in both bone resorption area and bone resorption depth (Fig 3C-F). Consistent with these results, type I collagenolysis as assessed by CTX-I generation (Garnero *et al*, 2003), is increased almost 1.5-fold in *Zeb1*$^{\Delta M/\Delta M}$ osteoclast cultures (Fig 3G). While intracellular acidification of *Zeb1*$^{\Delta M/\Delta M}$ osteoclasts appears unaffected by acidic orange staining (Appendix Fig S2B and C), a striking size increase in actin ring structure is noted when *Zeb1*$^{\Delta M/\Delta M}$ cells are cultured atop bone (Fig 3H and I). Neither the number of nuclei per osteoclast nor the number of actin rings per osteoclast on bone are altered in *Zeb1*$^{\Delta M/\Delta M}$ cells (Appendix Fig S2D and E), indicating actin ring size is the dominant phenotypic change observed in *Zeb1*$^{\Delta M/\Delta M}$ osteoclasts. Further, while αvβ3 integrin is generally regarded as the major receptor in osteoclasts mediating signaling cascades upstream of c-Src activation (Feng *et al*, 2001; Nagai *et al*, 2013; Sanjay *et al*, 2001; Zou *et al*, 2007), surface β3 integrin (CD61) levels as well as vitronectin-induced c-Src phosphorylation are unaffected in *Zeb1*$^{\Delta M/\Delta M}$ osteoclasts (Appendix Fig S2F-H).

Finally, to rule out the possibility that defects in *Zeb1*-targeted osteoclast function arise at early stages of monocyte-to-macrophage differentiation (i.e., Zeb1 is deleted in bone marrow-derived myeloid cells using *Csf1r-Cre* targeting strategy *in vivo*), macrophages were prepared from *Zeb1*$^{f/f}$ mice and then transduced *in vitro* with a lentiviral Cre expression vector just prior to osteoclastogenic induction (Appendix Fig S3A and B). Under these conditions, bone resorption and osteoclast sealing zone formation, but not osteoclastogenesis, are again increased (Appendix Fig S3C-E). Furthermore, ectopic expression of Zeb1 reverses the hyperactivation of bone resorptive activity and sealing zone formation in *Zeb1*-deficient osteoclasts (Appendix Fig S3F-I), thus confirming that deletion of Zeb1 is responsible for the enhanced osteoclast activity. Hence, Zeb1 plays a required and modulatory, late-stage role in controlling osteoclastic bone resorption.

Zeb1 regulates osteoclastic MtCK1 expression

To begin identifying potential Zeb1 targets capable of regulating bone resorbing activity, we conducted a transcriptome analysis comparing the expression profiles of wild-type versus *Zeb1*$^{\Delta M/\Delta M}$ osteoclasts. Using a minimum of 1.5-fold change as cutoff and an adjusted *P* value of <0.05, *Zeb1* deletion alters the expression of 510 unique transcripts reflecting 201 and 309 genes that are up- and down-regulated, respectively, in *Zeb1*$^{\Delta M/\Delta M}$ osteoclasts relative to controls (Fig 4A). Given that Zeb1 is classically characterized as a transcriptional repressor (Stemmler *et al.*, 2019; Vandewalle *et al.*, 2009), we noted that among the top 10 upregulated genes in knockout cells, the mitochondrial creatine kinase gene *Ckmt1*, encoding the enzyme MtCK1 critical to mitochondrial oxidative activity and energy metabolism (Schlattner *et al*, 2006; Wallimann *et al*, 2011; Wallimann *et al*, 1992), is the most highly expressed transcript in *Zeb1*$^{\Delta M/\Delta M}$ osteoclasts (Fig 4A and B). On the basis of DAVID Gene Ontology (GO) analysis, we further found that several important biological processes, such as DNA binding, ATP-binding, mitochondrion and cytoskeleton are enriched as the main altered categories defined by the pattern of differentially expressed genes (Fig 4C).

Osteoclast activation and bone resorption are energy-consuming processes supported by high metabolic activities (Arnett & Orriss, 2018; Indo *et al.*, 2013; Li *et al.*, 2020). Interestingly, RANKL stimulates mitochondrial creatine kinase activity and induces coordinated expression of genes associated with creatine metabolism, including creatine kinases (*Ckmt1* and *Ckb*) and the creatine transporter, *Slc6a8*, but not the gene products controlling creatine synthesis (*Gatm* or *Gamt*) (Fig 4D; Fig EV3A). We validated that *Zeb1*$^{\Delta M/\Delta M}$ osteoclasts display markedly increased *Ckmt1* levels with no changes in mRNA levels of *Ckb* or *Slc6a8* (Fig 4E; Fig EV3B). Consistent with these findings, levels of mitochondrial-localized MtCK1 are likewise increased in *Zeb1* knockout osteoclasts while MtCK1 expression is restored to normal levels following reintroduction of *Zeb1* using lentiviral transduction (Fig 4F-H; Appendix Fig S4A-C; Fig EV3C). Importantly, upregulated MtCK1 expression is not limited to *in vitro*-differentiated mouse osteoclasts as immunofluorescence analysis confirmed increased expression levels of MtCK1 in femur osteoclasts of *Zeb1*$^{\Delta M/\Delta M}$ mice while *ZEB1* targeting in human osteoclasts likewise increases MtCK1 expression by both western blot and immunofluorescence (Fig EV3D-H; Appendix Fig S4D).

Zeb1 preferentially associates with either E-box elements (5'-CAGGTG-3', 5'-CACCTG-3', or 5'-CATGTG-3') or Z-box elements (5'-TACCTG-3' or 5'-CAGGTA-3') in the promoter region of target genes (Guo *et al*, 2021; Larsen *et al*, 2016; Postigo & Dean, 1999; Rosmaninho *et al*, 2018). In this regard, a *de novo* search for DNA-enriched Zeb1 binding motifs demonstrates that both the mouse *Ckmt1* and human *CKMT1* promoter sequences contain multiple E-box and Z-box binding sites (Fig 4I). Indeed, using a *Ckmt1* reporter construct, luciferase activity is significantly repressed in the RANKL-stimulated macrophage cell line, RAW 264.7, following co-transfection with a ZEB1-expression vector (Fig 4J). Chromatin immunoprecipitation (ChIP) analysis confirms that an anti-Zeb1 antibody, but not its respective matched IgG control, immunoprecipitates a region of the *Ckmt1* promoter containing the Zeb1 binding site in wild-type osteoclasts relative to *Zeb1*-depleted cells (Fig 4K). Together, these results indicate that MtCK1 is a direct transcriptional target of Zeb1 in wild-type osteoclasts.

Independent of *Ckmt1*, we noted that *Epcam* (Epithelial cell adhesion molecule) is also among the top 10 differentially expressed genes in *Zeb1*$^{\Delta M/\Delta M}$ osteoclasts (Fig 4A and B). Though recent studies indicate that EpCAM can confer a survival advantage and differentiation block in *Zeb1*$^{-/-}$ hematopoietic stem cells (Almotiri *et al*, 2021), *Zeb1* deletion did not affect EpCAM protein expression in osteoclasts (Appendix Fig S4E and F). Of note, Zeb1 has been reported to regulate reactive oxygen species (ROS) production (de Barrios *et al*, 2019; Han *et al*, 2021; Han *et al*, 2022; Morel *et al*, 2017; Zhang *et al*, 2022) and nicotinamide adenine dinucleotide phosphate oxidase (NADPH) oxidases (mainly Nox2 and Nox4)-derived ROS are known to regulate osteoclast differentiation (Goettsch *et al*, 2013; Kang & Kim, 2016; Lee *et al*, 2005; Schroder, 2019). Nevertheless, ROS and H_2O_2 production levels are comparable between wild-type and *Zeb1*$^{\Delta M/\Delta M}$ osteoclasts (Appendix Fig S4G and H) while transcript levels of *Cybb* (encoding Nox2) and *Nox4,* as well as *Slc16a4* and *Gpx4*, are indistinguishable between wild-type and *Zeb1*-deficient cells (Appendix Fig S4I).

Zeb1 controls osteoclast energy metabolism

Creatine kinases are a family of enzymes that rapidly and reversibly transfer phosphoryl moieties between ATP and creatine to generate creatine phosphate, a highly diffusible, high-energy phosphate molecule important for maintaining cellular energy homeostasis (Schlattner *et al.*, 2006; Wallimann *et al.*, 2011; Wallimann *et al.*, 1992). Recently, MtCK1 has been reported to increase both total creatine and phosphocreatine levels in tumor cells (Fenouille *et al*, 2017; Kurmi *et al*, 2018). Consistent with these findings, *Zeb1*-null osteoclasts likewise display a significant increase in the level of phosphocreatine as well as their phosphocreatine/creatine (PCr/Cr) ratio relative to wild type controls (Fig 5A). As MtCK1 activity is further coupled to oxidative phosphorylation through the ATP/ADP carrier (Fenouille *et al.*, 2017; Kurmi *et al.*, 2018; Schlattner *et al.*, 2006; Wallimann *et al.*, 2011; Wallimann *et al.*, 1992), the increased creatine kinase-dependent phosphocreatine energy shuttle found in *Zeb1*-null osteoclasts would be predicted to dissipate the mitochondrial ATP pool to drive ADP-dependent respiration. While RANKL is known to induce shifts in mitochondrial mass and mtDNA copy number (Arnett & Orriss, 2018; Lemma *et al*, 2016; Zeng *et al.*, 2015), each of these endpoints are indistinguishable between wild-type and *Zeb1*$^{\Delta M/\Delta M}$ osteoclasts (Appendix Fig S5A-SD). Further, as assessed by Western blotting, *Zeb1*$^{\Delta M/\Delta M}$ osteoclasts express comparable levels of mitochondrial complexes I, II, III, IV and V with respect to control cells (Appendix Fig S5E and F). Nevertheless, *Zeb1*$^{\Delta M/\Delta M}$ osteoclasts display an increased basal mitochondrial respiration as well as maximal respiratory capacity after uncoupling oxygen consumption from mitochondrial ATP production with carbonyl cyanide p-(trifluoromethoxy)phenylhydrazone (FCCP), while the oxygen consumption rate (OCR) falls to basal levels with the addition of the mitochondrial ATP synthase and oxidative-phosphorylation inhibitor, oligomycin A (Fig 5B and C). In keeping with the higher respiratory activity observed in *Zeb1*-null osteoclasts that occurs in the absence of obvious changes in mitochondrial structure (Fig 5D), ATP levels are likewise significantly increased in the knockout cells (Fig 5E). Cellular energetics strongly correlates with Rho GTPase activity (Chen *et al*, 2018; Holmes *et al*, 2020; Wu *et al*, 2021; Zhang *et al*, 2013) which also serves as a critical determinant of actin ring and sealing zone formation (Teitelbaum, 2011; Touaitahuata *et al*, 2014; Uehara *et al*, 2017; Weivoda & Oursler, 2014). Consistent with a potential link between increased ATP levels and Rho GTPase activity, RhoA activity is also increased 2-fold in knockout osteoclasts (Fig 5F).

Zeb1-dependent regulation of MtCK1 activity drives osteoclast activation

As Zeb1-dependent regulation of MtCK1 activity correlate with changes in osteoclast energy metabolism, we sought to determine whether MtCK1 overexpression in wild-type osteoclasts alone would functionally recapitulate the *Zeb1*$^{\Delta M/\Delta M}$ osteoclast phenotype. As such, control osteoclasts were transduced with lentiviral expression vectors encoding either wild-type or a mutant form of MtCK1 lacking catalytic activity (MtCK1^{C316G}) (Fenouille *et al.*, 2017; Furter *et al*, 1993) (Fig 6A and B). Expression of cytosolic creatine kinase, Ckb, the mitochondrial markers, Tomm20 and VDAC, or Zeb1, as well as the osteoclast maturation markers, c-Src and Ctsk, remain unaltered following transduction with either construct (Fig 6C; Appendix Fig S5G). By contrast, transduction with wild-type MtCK1, but not MtCK1^{C316G}, increases mitochondrial creatine kinase activity, PCr/Cr ratios, mitochondrial respiration, ATP, and active RhoA levels to a degree similar, if not identical, to those observed in *Zeb1*$^{\Delta M/\Delta M}$ osteoclasts (Fig 6D-I). In coordinated fashion, increasing MtCK1 expression enhances both actin ring formation and bone-resorbing activity of transduced osteoclasts (Fig 6J and K). Further underlining the importance of phosphocreatine in mediating these effects, the addition of exogenous phosphocreatine alone to wild-type osteoclasts significantly increases GTP-loaded RhoA activity, actin ring formation as well as bone resorbing activity (Fig EV4A-D) in tandem with enhanced mitochondrial respiration and ATP production (Appendix Fig S6A-C). Next, to assess the relative importance of RhoA in controlling osteoclast activation driven by phosphocreatine, cells were next treated with the RhoA inhibitor, Y16 (Shang *et al*, 2013). Under these conditions, sealing zone formation and bone-resorptive activity by phosphocreatine-treated osteoclasts are each significantly downregulated by the RhoA inhibitor (Appendix Fig S6D and E). In a consistent fashion, while cellular energetics strongly correlate with Rho GTPase activity and cytoskeletal organization in other cell types (Chen *et al.*, 2018; Holmes *et al.*, 2020; Wu *et al.*, 2021; Zhang *et al.*, 2013), the mitochondrial ATP synthase inhibitor, oligomycin A, significantly reduces RhoA activity, sealing zone formation and bone resorption levels of phosphocreatine-treated wild-type osteoclasts (Appendix Fig S6F-H). Taken together, these data support a model wherein mitochondrial respiration and RhoA activation are intertwined with phosphocreatine's ability to regulate osteoclast activity.

Conversely, while targeting MtCK1 expression in *Zeb1*$^{\Delta M/\Delta M}$ osteoclasts with either of 2 structurally distinct shRNA constructs (sh*Ckmt1*) in *Zeb1*$^{\Delta M/\Delta M}$ BMDMs does not affect osteoclast maturation (Fig EV4E; Appendix Fig S7A), mitochondrial creatine kinase activity, cellular PCr/Cr ratios, mitochondrial respiration, and ATP levels are significantly downregulated in *Zeb1*$^{\Delta M/\Delta M}$ osteoclasts upon sh*Ckmt1* transduction to a level similar to that observed in wild-type osteoclasts (Fig EV4F-H). In turn, RhoA activity, actin ring formation and bone-resorbing activity are significantly inhibited in *Zeb1*-null osteoclasts after MtCK1 knockdown (Fig EV4I-K). Though Zeb1 has also been reported to regulate cancer cell metabolism via transcriptionally repressing the mitochondrial-localized deacetylase, *Sirt3*, or upregulating transcript levels of glycolytic enzymes, including *Pfkm*, *Hk2*, *Pfkp*, and *Pkm2* (Jiang *et al*, 2022; Xu *et al*, 2018; Zhou *et al*, 2021), gene expression levels of these enzymes are unaffected in *Zeb1*-deficient osteoclasts (Appendix Fig S7B).

Creatine kinase is a downstream effector of Zeb1-null human osteoclasts and mouse osteoclasts *ex vivo*

Given potential functional differences between mouse and human myeloid-derived cell populations (Ginhoux & Jung, 2014), we next sought to assess the status of the ZEB1/MtCK1 axis in human osteoclasts. As such, human monocyte-derived osteoclasts were cultured atop bone slices following transfection with either control siRNAs or constructs directed against either *ZEB1* or *CKMT1*. In the presence of si*ZEB1*, osteoclastogenesis proceeds in normal fashion with unaltered c-SRC and CTSK expression (Fig EV3E and F). By contrast, in response to *ZEB1* targeting, MtCK1 expression and kinase activity increase in tandem with an elevated cellular PCr/Cr ratio, higher ATP levels and RhoA activity with augmented mitochondrial respiration (Fig EV3E-H; Fig 7A-F). Correspondingly, actin ring/sealing zone formation and bone resorption are markedly enhanced (Fig 7G and H). Alternatively, si*CKMT1* delivery significantly inhibits RhoA activity, sealing zone formation and bone resorbing activity of human osteoclasts in concert with decreased mitochondrial creatine kinase activity, cellular PCr/Cr ratios and mitochondrial respiration (Fig EV5B-I; Appendix Fig S7C). Hence, human osteoclasts – like their mouse counterparts – employ the ZEB1/MtCK1 metabolic axis as a critical regulator of the bone resorptive phenotype.

Finally, to assess the importance of the creatine kinase axis in driving the hyperactive bone resorptive axis in Zeb1-null osteoclasts *ex vivo*, calvarial organ cultures were established from wild-type and null mice, respectively (Bellido & Delgado-Calle, 2020; Inada *et al*, 2004). Consistent with our *in vivo* results, confocal imaging of *Zeb1*$^{\Delta M/\Delta M}$ calvarial cultures coupled with quantitative analysis confirmed comparable osteoclast numbers as assessed by Vpp3 staining and TRAP activity along with increased actin ring formation and bone collagen degradation (Fig 7I-L). Importantly, the hyperactive bone resorptive phenotype in *Zeb1*$^{\Delta M/\Delta M}$ calvaria as well as the enhanced ring formation are both significantly inhibited by the treatment with the creatine kinase inhibitor, cyclocreatine, *ex vivo* (Fig 7I-L) or *in vitro* with *Zeb1*$^{\Delta M/\Delta M}$ osteoclasts (Fig EV5I). Together, these data demonstrate that Zeb1/MtCK1 axis confers osteoclasts with the essential transcriptional-metabolic regulatory machinery that is crucial to controlling bone resorption *in situ*.

Discussion

The unique capacity of osteoclasts to resorb bone - in both physiologic and pathologic contexts, highlights the importance for identifying the molecular mechanisms controlling their development and activity (Compston *et al.*, 2019; Zaidi, 2007). Though effects of EMT TFs remain predominately, but not solely, assigned to epithelial and mesenchymal cell populations (Francou & Anderson, 2020; Nieto *et al.*, 2016; Stemmler *et al.*, 2019; Vandewalle *et al.*, 2009), we report that osteoclasts - despite their myeloid origin - specifically express one EMT TF, i.e., Zeb1, both during and after differentiation, emphasizing their ability to function outside of classic EMT-related programs. Further, our study demonstrates that Zeb1 plays unexpected roles in orchestrating the activity of the bioenergetic machinery critical to mouse as well as human osteoclast function. In the absence of Zeb1, osteoclasts increase their phosphocreatine energy shuttle and mitochondrial respiration, resulting in a hyperactive, bone-resorbing phenotype. These findings further raise the possibility that osteoclasts respond to exogenous signals to autoregulate their Zeb1 levels to up- or down- regulate bone resorptive activity accordingly. Indeed, we find that osteoclasts cultured atop plastic substrata decrease Zeb1 expression when transplanted atop bone coincident with the initiation of active resorption (Appendix Fig S8A-D).

With regard to bone metabolism, early studies demonstrated that global *Zeb1* deletion elicits major skeletal abnormalities, along with perinatal lethality (Takagi *et al*, 1998). Interestingly, Zeb1 is expressed in proliferating mesenchymal progenitors, and Zeb1 mutant mice display cleft palate and defective nasal formation along with other craniofacial abnormalities (Bellon *et al*, 2009; Liu *et al*, 2008; Takagi *et al.*, 1998). Zeb1 is markedly downregulated during osteoblastic differentiation and its depletion results in the premature differentiation of mesenchymal stem cells (Ruh *et al*, 2021). Zeb1 can also affect bone development in a non-cell autonomous fashion with the finding that endothelial cell-specific deletion of Zeb1 impairs CD31^{hi}endomucin^{hi} vessel formation in the bone, resulting in reduced osteogenesis (Fu *et al*, 2020). Finally, independent of bone-specific phenotypes, Zeb1 has only recently been shown to coordinate self-renewal and multi-lineage differentiation fates of hematopoietic stem cells while also affecting both T cell and macrophage development (Almotiri *et al.*, 2021). Despite the assignment of new functions to Zeb1, a link to mitochondrial energy metabolism has not been proposed previously. Interestingly, Zeb1 protein levels are detected as early as day 2 of the osteoclastogenic program while MtCK1 begins to be expressed at day 4 (Fig 3B and 4F; Appendix Fig S2A and S4A), suggesting that MtCK1 is induced by other unknown transcription factors during osteoclast differentiation.

To initiate the bone resorption process, osteoclasts reorganize cytoskeletal structure to form an F-actin rich sealing zone that anchors the cells to the bone surface and creates a confined resorption microenvironment where protons and bone-degrading enzymes are delivered (Blangy *et al.*, 2020; Boyle *et al.*, 2003; Teitelbaum, 2011; Teitelbaum & Ross, 2003; Zhu *et al.*, 2020). As such, osteoclasts are in a state of high-energy demand that is characterized by abundant mitochondria, elevated expression of oxidative phosphorylation-associated enzymes and high rates of oxygen consumption (Arnett & Orriss, 2018; Bae *et al.*, 2017; Lemma *et al.*, 2016; Li *et al.*, 2020; Zeng *et al.*, 2015). Nevertheless, how mitochondrial energy metabolism is regulated and how mitochondrial bioenergetics and substrate utilization cooperatively coordinate osteoclast cytoskeletal organization and activation in concert with transcriptional machinery is poorly understood. Previous work has demonstrated that the energy required for osteoclast differentiation mainly derives from mitochondrial oxidative metabolism, whereas the cellular activities associated with bone resorption per se are alternatively supported by glycolysis (Lemma *et al.*, 2016). By contrast, more recent studies demonstrated that mitochondrial biogenesis is not required for osteoclastogenesis *per se*, but instead for sealing zone assembly and bone resorbing activity (Ling *et al*, 2021; Nakano *et al*, 2019; Zhang *et al*, 2018). In this latter scenario, the bone-resorptive capacity of individual osteoclasts was enabled by the transcriptional co-activator PGC1β, G-protein Gα13, or the mitochondrial deacetylase, Sirt3, which controlled both mitochondrial biogenesis and the oxidative phosphorylation-mediated cytoskeletal organization critical to sealing zone formation (Ling *et al.*, 2021; Nakano *et al.*, 2019; Zhang *et al.*, 2018). Contrasting with these studies, Zeb1 neither regulates osteoclast differentiation nor mitochondrial biogenesis. Instead, Zeb1 functions as a transcriptional repressor of MtCK1, thereby controlling the phosphocreatine shuttle, mitochondrial respiration and ATP production to finally modulate bone resorptive activity. Importantly, increasing MtCK1 expression alone in wild-type osteoclasts was sufficient in mediating the reprogramming of mitochondrial activity and enhancing bone resorption, suggesting that MtCK1 is a central effector of osteoclast activation.

Phosphorylated guanidine compounds, known as phosphagens, are linked to ATP hydrolysis and temporal buffering when cells experience dynamic energy requirements. Among the phosphagens, the phosphocreatine–creatine kinase axis is one of the most well-studied, perhaps owing to its extensive tissue distribution in vertebrates (Kazak & Cohen, 2020; Schlattner *et al.*, 2006; Wallimann *et al.*, 2011; Wallimann *et al.*, 1992). The phosphocreatine–creatine kinase system operates in cell types with dynamic rates of energy turnover, such as neurons, muscle and spermatozoa, where it reversibly catalyzes the phosphorylation of creatine to phosphocreatine, an energy-storage molecule. In elongated-cell systems, such as muscle and motile gametes, the phosphagen system increases the free energy of ATP hydrolysis by steepening the gradient between local ATP and ADP. Also, the phosphagen system can overcome diffusion barriers between the source of ATP (mitochondria) and the site where ATP is consumed (Schlattner *et al.*, 2006; Wallimann *et al.*, 2011; Wallimann *et al.*, 1992). Interestingly, thermogenic fat tissues were recently revealed to employ a futile cycle of creatine and phosphocreatine to dissipate energy and stimulate mitochondrial ATP demand, thereby promoting cold adaptation (Kazak *et al*, 2015; Kazak *et al*, 2017; Kazak & Cohen, 2020). Mitochondrial creatine kinase, together with cytosolic creatine kinase isozymes and phosphocreatine, provide a temporal and spatial energy buffer to maintain cellular energy homeostasis (Schlattner *et al.*, 2006; Wallimann *et al.*, 2011; Wallimann *et al.*, 1992). MtCK1 is a mitochondrial protein that facilitates the phosphocreatine energy shuttle by transferring a phosphate group from mitochondrial ATP to creatine which readily passes through the mitochondrial membrane, plays an important role in maintaining adequate phosphoryl energy reserves during energy fluxes in metabolically active cells (Schlattner *et al.*, 2006; Wallimann *et al.*, 2011; Wallimann *et al.*, 1992). Interestingly, we detected a sharp increase of the expression of a *Slc6a8/Ckmt1/Ckb* triad during macrophage-osteoclast transition. It is intriguing that osteoclasts appear to be actively employing creatine metabolism based on the gene expression signature of the creatine transporter and creatine kinases, MtCK1 and Ckb, but not creatine-synthetic enzymes. It has been reported earlier that *Ckb* knockout suppressed the bone-resorbing activity of osteoclasts *in vitro* without affecting cellular ATP levels (Chang *et al*, 2008). While Ckb has recently been reported to traffic into mitochondria using an internal mitochondrial targeting sequence in brown fat (Rahbani *et al*, 2021), we find no evidence for Ckb expression in the mitochondria of either wild-type or *Zeb1*-deleted osteoclasts. Of note, two recent reports identified MtCK1 as a potential therapeutic target in cancer cells on the basis of its ability to serve as a core high-energy phosphate transfer system that regulates mitochondrial respiration, ATP production and cell growth (Fenouille *et al.*, 2017; Kurmi *et al.*, 2018). While Zeb1 has been reported to affect glucose and fatty acid metabolism in normal and neoplastic epithelial cells (Masin *et al*, 2014; Mathow *et al*, 2015; Xu *et al.*, 2018; Zhang *et al.*, 2016), our studies suggest that MtCK1 and mitochondrial activity could be critical targets in a variety of cell populations. Interestingly, a recent study described the ability of Zeb1 to regulate rat osteoclast activity by targeting the DNA polymerase interacting protein, PLODIP2, and of direct relevance to our own findings, that decreased levels of Zeb1 can be found in mononuclear cells recovered from osteoporotic women (Zhu *et al.*, 2022). However, distinguishing our work from theirs, PLODIP2 expression was unaffected in our RNA-seq data of wild-type vs *Zeb1* knockout osteoclast's. Likewise, Zeb1 has been reported to regulate mitochondrial mass and fusion in hematopoietic stem cells by repressing mitofusin-2 expression (Zhang *et al*., 2022), but similar effects were not noted in our studies highlighting the fact that Zeb1 functions are cell- as well as context- dependent. Indeed, while Zeb1 undoubtedly plays discrete roles in a diverse set of other cell populations (Almotiri *et al.*, 2021; Feldker *et al*, 2020; Krebs *et al*, 2017; Morel *et al.*, 2017; Stemmler *et al.*, 2019; Vandewalle *et al.*, 2009), our data clearly demonstrate that the osteoclast hyper-resorptive phenotype observed here can be ascribed to MtCK1 targeting and mitochondrial energy metabolism.

In summary, we have identified Zeb1 as a key upstream regulator of metabolic reprogramming during osteoclast activation and demonstrated the importance of a previously unrecognized Zeb1/MtCK1 axis as an integrator of mitochondrial signaling and osteoclast-dependent bone resorption, potentially identifying new targets for therapeutic intervention in pathological bone-resorptive states. While Zeb1 is considered undruggable (Francou & Anderson, 2020; Nieto *et al.*, 2016; Stemmler *et al.*, 2019; Vandewalle *et al.*, 2009), directly targeting downstream effectors, such as MtCK1, is deserving of consideration.

Materials and Methods

Mouse strains

Mice harboring *Zeb1-floxed* alleles (*Zeb1*$^{f/f}$) were generated as previously described and were maintained on a C57BL/6J genetic background (Brabletz *et al*, 2017), while *Csf1r-Cre* mice (FVB/NJ background) obtained from Jackson Laboratories (Zhu *et al.*, 2020) were backcrossed onto a C57BL/6J background (n>10 generations). *Zeb1*$^{f/f}$ mice were bred with *Csf1r-Cre* transgenic mice to obtain *Zeb1*$^{\Delta M/\Delta M}$ (*Csf1r-Cre*/*Zeb1*$^{f/f}$) mice. *Zeb1*$^{+/+}$ mice are defined as "wild-type" control while *Zeb1*$^{f/+}$ and *Zeb*$^{f/f}$ mice, which uniformly display normal bone and osteoclast phenotypes, are described as such in the text and are considered 'control' mice. For genotyping primers, see Appendix Table S1. All mice were housed under 12-h light/12-h dark cycle (6 a.m.–6 p.m.) with a standard rodent chow diet. Throughout, mice were age-matched and then randomly assigned to minimize the effects of subjective bias. All mouse work was performed under the guidelines and approval of the Animal Welfare and Ethics Committee (School and Hospital of Stomatology, Wuhan University) and the University of Michigan Institutional Animal Care & Use Committee (IACUC).

In vitro osteoclast differentiation

Mature osteoclasts were generated as described (Tang *et al.*, 2009; Zhu *et al.*, 2020). Briefly, bone marrow cells extracted from femurs or tibiae of 10- to 12-wk old male mice were cultured in α-MEM containing 10% FBS, 100 IU/ml penicillin, and 100 μg/ml streptomycin with 20 ng/ml recombinant M-CSF (R&D Systems) in plastic petri dishes. Cells were incubated at 37 °C in 95% air/5% CO_2 for 4 d and then lifted with 5 mM EDTA in PBS. Recovered BMDMs were cultured in α-MEM containing 10% FBS supplemented with 10 ng/ml M-CSF and 20 ng/ml RANKL (R&D Systems) for 5 days in tissue-culture dishes to induce osteoclast formation. Mature osteoclasts were characterized by staining for TRAP activity using an Acid Phosphatase Leukocyte Kit (Sigma-Aldrich), and TRAP-positive multinucleated cells (>3 nuclei/cell) counted.

RNA extraction, qPCR and RNA-seq analysis

RNA was isolated from cultured cells with TRIzol reagent (Invitrogen) and purified using QIAGEN RNeasy Mini-kit columns (QIAGEN). RNA quality was confirmed using an Agilent 2100

Bioanalyzer. Mouse complementary DNA (cDNA) was reverse-transcribed from 1 µg total RNA with SuperScript VILO Master Mix (Life Technologies). qPCR was performed in triplicate samples using SYBR Green PCR master mix (Applied Biosystems) according to the manufacturer's instructions. For each transcript examined, mRNA expression was normalized to *Gapdh/GAPDH*. For qPCR primers, see Appendix Table S2.

For RNA-seq, the construction of libraries was generated using QuantSeq 3' mRNA-Seq Library Prep Kit (Lexogen) according to the manufacturer's instructions. High-throughput sequencing was performed as single-end 75 sequencing using NextSeq 500 (Illumina). Each sample was analyzed at the University of Michigan Advanced Genomics Core. Data were aligned using the STAR aligner and featureCounts v1.6.4 software, and reads per kilobase of transcript per million mapped read values on gene level were estimated for ensemble transcriptome (Dobin *et al*, 2013; Liao *et al*, 2014). DESeq2 was used to estimate significance between any two experimental groups (Love *et al*, 2014). Principal component analysis was performed on the RNA-Seq data to visualize sample-to-sample variance. Genes with a fold change of 1.5 were considered as differentially expressed genes and analyzed using the DAVID Bioinformatics Resources 6.8 (Jiao *et al*, 2012).

Western blot analysis

Cell lysate preparation, sodium dodecyl sulfate-polyacrylamide gel electrophoresis (SDS-PAGE) and Western blotting were carried out according to standard protocols. Proteins were harvested in cell lysis buffer supplemented with proteinase inhibitor cocktail (Sigma-Aldrich) and phosphatase inhibitor cocktail 2 (Sigma-Aldrich). Antigen detection was performed using antibodies directed against Zeb1 (Sigma-Aldrich, HPA027524), c-Src (Cell Signaling, #2109), Ctsk (Santa Cruz, sc-48353), NFATc1 (Santa Cruz, sc-7294), c-Fos (Cell Signaling, #2250), β3 integrin (Cell Signaling, #4702), Mmp9 (Abcam, ab38898), Mmp14 (Abcam, ab51074), MtCK1 (Proteintech, 15346-1-AP), Ckb (Abcam, ab108388), VDAC (Cell Signaling, #4866), Tomm20 (Millipore, MABT166), OXPHOS (Abcam, ab110413), Vinculin (Sigma-Aldrich, V9131) or β-actin (Cell Signaling, #4970). Bound primary antibodies (diluted to 1:1,000) were detected with horseradish peroxidase-conjugated species-specific secondary antibodies (Santa Cruz; diluted to 1:2,000) using the Super Signal Pico system (Thermo Fisher Scientific).

Immunofluorescence staining

For immunofluorescent staining, osteoclasts were fixed with 4% paraformaldehyde, permeabilized with 0.1% Triton X-100, and blocked for 1h prior to an overnight incubation at 4°C with primary antibodies directed against Zeb1 (Sigma-Aldrich, HPA027524), TRAP (Santa Cruz, sc-30833), or MtCK1 (Proteintech, 15346-1-AP). For F-actin staining, osteoclasts were permeabilized with 0.1% Triton X-100 and incubated with TRITC- or Alexa Fluor 647-conjugated phalloidin (Invitrogen). For Mitotracker Green staining, non-fixed cells were incubated with 100 nM Mitotracker Green (Invitrogen, M7514) in HBSS for 20 min. For bone tissue immunofluorescence, femurs from 8-wk old were fixed in 4% paraformaldehyde at 4°C overnight, decalcified in 10% EDTA and transferred to 30% sucrose in PBS for embedding in OCT (Fisher Healthcare). Frozen sections were permeabilized with 0.3-0.5% Triton X-100 in PBS, and blocked for 2 h prior to adding primary antibodies directed against Zeb1 (Sigma-Aldrich, HPA027524) or MtCK1 (Proteintech, 15346-1-AP) with TRAP (Santa Cruz, sc-30833). Following primary antibody incubations, sections were incubated with Alexa Fluor 488- or Alexa Fluor 594-conjugated secondary antibodies (Invitrogen Molecular Probes). Nuclei were visualized by staining with 1 µg/ml 4',6-diamidino-2-phenylindole (DAPI). Fluorescence images were acquired with a Nikon A1 laser-scanning confocal microscope and analyzed with Adobe Photoshop and Image J software.

Single cell RNA-seq analysis

Single cell RNA-seq analysis was performed utilizing a publicly available Gene Expression Omnibus (GEO) dataset (Data ref: Yahara *et al.*, 2020) under accession number GSE125088 (Yahara *et al.*, 2020). Briefly, R package Seurat Version 3.2.2 (http://satijalab.org/seurat/) was utilized to perform secondary statistical analysis and generate visualizations of the data. More specifically, subset analysis was performed where cells were excluded which contained greater than 15% expression of mitochondrial genes and RNA between 200-6000. Data was then normalized, scaled and 200 variable features were found using a variance-stabilizing transformation method. One hundred replicates were considered using principal component analysis and Jackstraw was scored to 20 dimensions (Macosko *et al*, 2015). Neighbors were calculated to 20 dimensions and clusters were determined at a resolution of 0.5 using the FindClusters function in Seurat. Differential expression of relevant cell marker genes was visualized on the *t*-SNE plot, which reduced the information captured in the selected significant principal components to two dimensions, to reveal specific individual cell types (Zhou & Jin, 2020). Differential expression of relevant cell marker genes was visualized on the t-SNE plot to reveal specific individual cell types.

Human osteoclast culture and RNA interference

Normal human CD14$^+$ monocytes (Lonza) were cultured in α-MEM supplemented with 10% FBS, 2 mM L-glutamine, 100 U/mL penicillin-streptomycin and 20 ng/ml M-CSF for 6 days to expand the precursor population and differentiate into macrophages. Cells were then detached with Accutase (Gibco) and seeded on tissue-culture plastic dishes or bone slices, and cultured with M-CSF (20 ng/ml) and RANKL (20 ng/ml) for 9 days to induce multinuclear osteoclast formation and bone resorption as previously described (Raynaud-Messina *et al.*, 2018; Zhu *et al.*, 2020). For RNA interference experiments, primary human macrophages were transfected with individual siRNA oligonucleotides using GenMute siRNA Transfection Reagent (SignaGen Laboratories) following the manufacturer's instructions (Aucher *et al*, 2013), which were then induced into human osteoclasts with M-CSF and RANKL. 2 independent siRNA specifically targeting *ZEB1* (109652 and 109653, Thermo Fisher Scientific), 2 independent siRNA targeting *CKMT1* (s3097 and s3099, Thermo Fisher Scientific), and the corresponding non-targeting control siRNA (sc-36869, Santa Cruz) were used. Expression of the siRNA knockdown efficiency was confirmed by Western blot.

Nano computed tomography (nanoCT) analysis

Excised mouse femurs as well as lumbar vertebrae were scanned using the nanotom M nanoCT (Phoenix X-ray, GE Measurement & Control; Wunstorf, Germany) as previously described (Khoury *et al*, 2015). Femurs and L3 vertebrae were scanned at an 8 μm isotropic voxel resolution, and calibrated three-dimensional images reconstructed and analyzed in Microview ABA 2.2. Bone morphometric variables were analyzed, including Bone Volume/Tissue Volume (BV/TV), Trabecular Number (Tb.N), Trabecular Separation (Tb.Sp), Trabecular Thickness (Tb.Th), and Cortical thickness (Ct.Th), as described previously (Khoury *et al.*, 2015; Tang *et al*, 2016; Zhu *et al.*, 2020).

Bone histomorphometry

Histology was performed as previously described (Tang *et al.*, 2016; Tang *et al.*, 2009; Zhu *et al.*, 2020). Briefly, the mice femurs were either fixed with 10% neutral buffered formalin followed by decalcification in 10% EDTA for 3 wks, paraffin embedding, and Hematoxylin/Eosin (H&E)

staining, or with 70% ethanol followed by plastic embedding and Golden trichrome staining. Femur osteoclasts were identified by staining for tartrate resistant acid phosphatase (TRAP) using an Acid Phosphatase Leukocyte Kit (Sigma-Aldrich). Osteoclastic and osteoblastic parameters were measured and analyzed using Bioquant OSTEO (Dempster *et al*, 2013). Mineral apposition rate was determined with double-calcein bone labeling as described (Tang *et al.*, 2009; Zhu *et al.*, 2020; Zou *et al.*, 2016).

In vivo markers of bone turnover

For bone resorption assays, the serum concentration of cross-linked C-telopeptide of type I collagen (CTX-I) was determined in overnight-fasted mice using the RatLaps CTX-I EIA kit (Immunodiagnostic Systems) according to the manufacturer's instructions. Osteoblast bone formation was monitored using the mouse Osteocalcin Enzyme Immunoassay kit (Alfa Aesar) according to the manufacturer's instructions.

In vitro bone resorbing activity

For bone resorption assays, BMDMs or pre-osteoclasts were seeded and cultured on bovine cortical bone slices (Immunodiagnostic Systems) in the presence of M-CSF and RANKL, as described previously (Wu et al., 2017; Zhang et al., 2018; Zhu et al., 2020). After the indicated culture period, bone slices were then incubated in 0.5 N NaOH for 30 seconds, and the cells scraped off using a cotton swab. Bone samples were sonicated in PBS, stained with 20 µg/ml WGA-lectin (Sigma-Aldrich) for 45 min and then incubated with 3,3'-diaminobenzidine (DAB) tablets (Sigma-Aldrich) for 15 min. The area resorbed was determined using Image J software. To analyze bone resorption pit depth, three-dimensional profiles of resorption pits were characterized using a reflective confocal laser scanning microscope (RCLSM) (Leica SP8). Quantitative analysis of resorption pit depth was performed using Imaris software (Bitplane). The concentration of the CTX-I was measured using the CrossLaps for Culture CTX-I ELISA kit (Immunodiagnostic Systems) according to the manufacturer's instructions.

Flow cytometry analysis

Single-cell suspensions of osteoclast precursor cells or mature osteoclasts were differentiated on petri dishes, detached and collected after passing through a 40 µm cell strainer (BD Bioscience), incubated with Fc block (eBioscience) for 10 min, and then incubated with Alexa Fluor 488-conjugated anti-CD11b M1/70 (eBioscience, 53-0112-80), BV711-conjugated CD326/EpCAM (Epithelial cell adhesion molecule; BD Bioscience, 563134), or the corresponding isotype control (eBioscience) in flow cytometry staining buffer (eBioscience) for 30 min at 4 °C. For Mitotracker Green staining, cells were incubated with 100 nM Mitotracker Green (Invitrogen, M7514) in HBSS for 45 min. For ROS level detection, cells were incubated with 20 μM DCFH-DA (Beyotime, S0033S) for 30min at 37 °C in the dark (Kalyanaraman *et al*, 2017; Murphy *et al*, 2022). Then, cells were subjected to flow cytometry analysis on a FACS Canto II (BD Bioscience).

Cell proliferation assay

Cells were seeded at 1 × 10^4 cells per well in 96-well plates and proliferation determined using the cell proliferation reagent, WST-1 (Sigma-Aldrich), according to the manufacturer's instructions.

Cell apoptosis assay

Apoptotic nuclei in cultured osteoclasts were identified by TUNEL staining using the In Situ Cell Death Detection Kit, Fluorescein (Roche) as previously described (Wu *et al*, 2017). Nuclei were visualized by staining with 1 μg/ml 4',6-diamidino-2-phenylindole (DAPI). Fluorescence images were acquired with a Nikon A1 laser-scanning confocal microscope and apoptotic nuclei were analyzed with Adobe Photoshop and Image J software.

Osteoclast acid production assay

Acid production was determined using acridine orange as described (Ferron *et al*, 2013). To assess intracellular pH, osteoclasts differentiated on cortical bone slices were incubated in MEM buffered at pH 7.4 with 20 mM HEPES and containing 5 μg/ml acridine orange (Invitrogen) for 15 min at 37°C, washed, and imaged using a confocal microscope (excitation, 488 nm; emission, 500–550 nm [green form] and 570–620 nm [red/orange acidic form]).

Mitochondrial fractionation and mitochondrial creatine kinase activity assay

Mitochondria-enriched fractions of BMMs and osteoclasts were isolated using a mammalian mitochondria isolation kit for cultured cells (BioVision) according to the manufacturer's instructions. The pelleted mitochondria were either lysed in the lysis buffer provided in the presence of protease inhibitors for western blot analysis or resuspended for subsequent creatine kinase activity assay (Rahbani *et al.*, 2021). Creatine kinase activity from isolated mitochondria was examined using the Creatine Kinase Activity Assay Kit (Sigma-Aldrich) according to the manufacturer's instructions.

Luciferase reporter assay

The *Ckmt1* promoter reporter construct has been described previously (Fenouille *et al.*, 2017). Mouse macrophage cell line RAW 264.7 (ATCC, TIB-71) was co-transfected with the *Ckmt1* promoter construct expressing Gaussia Luciferase and Secreted Alkaline Phosphatase (GeneCopoeia) and the Zeb1 plasmid using GenJet DNA Transfection Reagent (SignaGen Laboratories) in accordance with the manufacturer's protocol. Transfection medium was replaced by fresh medium containing RANKL about 6 h after transfection. After 48 hours of incubation, medium was collected for parallel bioluminescence assays of Gaussia luciferase and secreted alkaline phosphatase using Secrete-Pair Dual Luminescence Assay Kit (Genecopoiea), using a SpectraMax L (Molecular Devices) plate reader.

Chromatin immunoprecipitation (ChIP) assay

ChIP assay was carried out by using the SimpleChIP® Chromatin IP Kit (Cell Signaling) according to the manufacturer's instructions. Briefly, crosslinking was performed in cell culture medium containing 1% formaldehyde with gentle rotation for 10 min at room temperature. Fixation was stopped by the addition of glycine (125 mM final concentration). Fixed cells were then washed and digested by micrococcal nuclease. The nuclear pellet was suspended in chromatin immunoprecipitation (ChIP) buffer and sheared by sonication. The sheared chromatin was then immunoprecipitated with the Zeb1 antibody (Sigma-Aldrich, HPA027524) or the control IgG (Cell Signaling), bound to the Protein G Magnetic Beads. The immunoprecipitated chromatins were then eluted with ChIP elution buffer. The DNA fragments were released by treatment of ribonuclease A and then proteinase K at 65°C for 2 hours. The released DNA fragments were purified with columns and amplified by site-specific primers by qPCR. Five percent of the chromatin extract was set aside for input. All ChIP signals were normalized to the input. The following *Ckmt1* primers were used: 5'-AAGCGCTTTTCCAAATTTCC-3' (sense) and 5'-CCTGAGAAAGCTACTCTCCCTTT-3' (antisense).

H_2O_2 production assay

The level of H_2O_2 production was analyzed with a Hydrogen Peroxide Assay Kit (Beyotime) based on the ferrous oxidation-xylenol orange method, according to the manufacturer's instruction with minor modifications (Murphy *et al.*, 2022; Zhao *et al*, 2021). H_2O_2 production is detected extracellularly because hydrogen peroxide has a cell permeability coefficient similar to water and does not accumulate within intracellular compartments (Kalyanaraman *et al.*, 2017; Murphy *et al.*, 2022). Briefly, osteoclasts cultured on 6-well plates were washed without lysis and incubated with hydrogen peroxide detection reagent at room temperature. After 45 min of incubation, the supernatant was transferred to 96 well plates and then measured immediately with a microplate reader (Bio-Rad) at a wavelength of 570 nm. The H_2O_2 level was calculated using a standard curve generated with standard solutions of H_2O_2 and normalized to total protein levels determined with BCA assay.

Metabolite extraction and mass spectrometry analysis of phosphocreatine and creatine level

Intracellular metabolites were extracted from cells using 80% ice-cold methanol followed by centrifugation as previously described (Bian *et al*, 2020). Creatine and phosphocreatine were profiled at the University of Michigan Life Sciences Institute Mass Spectrometry Core. An Agilent LC/MS system was used consisting of the 1290 Infinity HPLC system and a Q-tof G6545A MS system equipped with a Dual Agilent Jet Stream Electrospray Ionization source. Poroshell 120 Hilic-OH5 column (Agilent Technologies) was used, which is 2.1x100mm and 2.7 micron particle size. The HPLC condition is as follows: Mobile Phase A is water in 0.1% formic acid; mobile phase B is 95% acetonitrile, 5% water, and 0.1% formic acid. The chromatographic method held the initial mobile phase composition (5% A) constant for 1 minutes, followed by a linear gradient to 90 % A over 4 minutes, and then held at 90% A for 3 minutes. The flow rate is set at 0.3 ml/min. Column was kept at room temperature. Sample injection volume is 20 µl. Data were collected in the positive mode. The following Q-tof operating parameters were used: capillary voltage: 3500 V; nebulizer pressure: 30 psig; drying gas: 11 L/min; gas temperature: 325°C; sheath gas flow: 11 L/min; sheath gas temperature: 275°C; nozzle voltage: 500 V; fragmentor voltage: 140 V; skimmer voltage: 65 V; octopole RF: 750 V. Post time between runs was set for 3 minutes. The mass spectra were recorded across the range of 50-1500 *m/z* at 2 GHz and a scan rate of 3 spectra/sec. Reference solution in Bottle A using reference nebulizer and reference mass correction were enabled. The reference solution contained reference masses purine C5H4N4 at *m/z* 121.0509 and HP-921 [hexakis-(1H,1H,3H-terafluoro-pentoxy)phosphazene] (C18H18O6N3P3F24) at *m/z* 922.0098. Both centroid and profile data were recorded. UV spectra were recorded in poly diode array (PDA) mode from 190 to 400 nm. The retention time and position of the peaks were confirmed using pure standard compounds freshly prepared in HPLC-grade water. Standard curves were obtained using known amounts of pure standard compound to calculate the detection range, accuracy and quantity. A known quantity of authentic pure standard compound was spiked into the sample to identity and quantify each metabolite of interest. Data Analysis was using Qualitative Analysis of MassHunter software (version 10.0).

Mitochondrial DNA (mtDNA) quantitation

mtDNA copy number per nuclear genome in osteoclasts was quantitated as described previously (Nakahira *et al*, 2011). Total DNA purification was performed using the DNeasy kit (Qiagen). The abundance of nuclear and mitochondrial DNA, reflected by 18s ribosomal RNA and cytochrome c oxidase I, was quantified by real-time PCR under standard conditions using a SYBR Green PCR kit (Qiagen). The ratios between mtDNA and nuclear DNA concentrations were calculated.

Transmission electron microscopy analysis

Cell pellets were fixed (2.5% glutaraldehyde in 0.1 M Sorensen's buffer, pH 7.2) and post-fixed with 1% osmium tetroxide prior to embedding in EMbed 812 epoxy resin (Electron Microscopy Sciences). Thin sections (70 nm) were post-stained with uranyl acetate and Reynolds lead citrate, and imaged with a JE0L JEM-1400 Plus electron microscope. Images were recorded digitally using a Hamamatsu ORCA-HR digital camera system, operated using AMT software (Advanced Microscopy Techniques Corporation).

Mitochondrial oxygen consumption (OCR) measurement

The mitochondrial respiratory activity was assessed by measuring oxygen consumption rate (OCR) of cells on a Seahorse XFe96 Analyzer (Agilent) using the Seahorse XF Cell Mito Stress test kit (Agilent) according to the manufacturer's instructions. Briefly, pre-osteoclasts were seeded on XFe96 cell culture microplates (Seahorse Bioscience) at a seeding density of 5×10^4 cells per well and stimulated with M-CSF and RANKL for 2 days. Before the assay, cells were rinsed twice and kept in pre-warmed XF assay medium (pH 7.4) supplemented with 1 mM sodium pyruvate, 2 mM glutamine, and 10 mM glucose in a 37°C non-CO_2 incubator for 1 h to allow for pre-equilibration with the assay medium. Next, the respiratory rate was measured at 37 °C in at least 3 replicates per condition by using the following perturbation drugs in succession: 1 μM oligomycin, 0.5-2 μM carbonyl cyanide p-(trifluoromethoxy)phenylhydrazone (FCCP), and 0.5 μM rotenone (ROT)/antimycin A (AA). The final FCCP concentration was optimized to achieve maximal respiration in each condition. The basal OCR was measured before drug exposure. We calculated the mitochondrial function metrics as described previously (Little *et al*, 2020). The measurement was normalized to the relative level of DNA determined by measuring the fluorescence intensity of cells stained by CyQuant NF dye (Molecular Probes).

ATP quantification assay

Intracellular ATP level was quantified using an ATP Determination Kit (Invitrogen). Briefly, reaction mixture was added to the 96-well cell culture plate, which contains the cultured cells or standard solution. After 20 min of incubation in the dark, the plate was read using a SpectraMax L (Molecular Devices) plate reader in the mode of luminescence detection. A standard curve for ATP was obtained with a series of dilution of the ATP standards and ATP-free water provided in the kit. Intracellular ATP level were calculated using the standard curve and normalized for cellular protein concentration.

Rho GTPase activity assay

Osteoclasts were starved for 4 hours in 2% FBS containing α-MEM, then then stimulated with 20 ng/ml M-CSF and 30 ng/ml RANKL for 15 min and lysed. Cell lysates was harvested and Rho GTPase activity was analyzed using RhoA G-LISA Activation Assay kits (Cytoskeleton) according to the manufacturer's instructions.

Lentiviral gene transduction and short hairpin RNA (shRNA) retroviral knockdown

Where indicated, BMDMs were transduced with either a control vector, wild-type human MtCK1, a metabolic inactive MtCK1^{C316G} mutant expression vector, a Cre vector, or a wild-type human ZEB1 expression vector. The catalytically-inactive MtCK1^{C316G} mutant harbors a Gly substitution at a critical Cys residue that is required for synergistic binding of MtCK1 to its substrate (Fenouille *et al.*, 2017; Furter *et al.*, 1993). The MtCK1, MtCK1^{C316G} mutant, and ZEB1 constructs were cloned into the pHAGE-CMV lentiviral vector, while the Cre construct was cloned into the pLentilox-IRES-GFP lentiviral vector (Zhu *et al.*, 2020). For knockdown of mouse *MtCK1*, 2 independent shRNA constructs (TF512727B and TF512727C, ORIGENE) and a single scrambled shRNA construct (TR30015, ORIGENE) cloned into the pRFP-C-RS retroviral vector were used. Expression of the recombinant proteins and shRNA knockdown efficiency was confirmed by Western blot.

Ex vivo calvarial organ cultures

Calvariae from 5-day-old wild-type or *Zeb1*$^{\Delta M/\Delta M}$ mice were isolated aseptically, cleaned, and cultured for 16 h at 37°C in 0.5 ml of BGJb medium (Life Technologies) containing 1 mg/ml BSA (fraction V, Sigma) as described previously (Inada *et al.*, 2004). Half calvariae were transferred to fresh medium with 50 nM PTH in the presence or absence of cyclocreatine (Cayman Chemical), and cultured for an additional 5 days. Culture supernatant was collected for bone resorption marker CTX-I level detection using RatLaps CTX-I EIA kit (Immunodiagnostic Systems). The half calvariae were either fixed for immunostaining or snap-frozen for TRAP activity assay.

Calvarial tissue lysate preparation and TRAP activity assay

The snap-frozen calvariae were extracted and TRAP activity was detected as previously described (Cackowski *et al*, 2010). After homogenization using a ground glass homogenizer in 200 µL of NP-40 lysis buffer (1% NP-40, 150 mM NaCl, 50 mM Tris, pH 8), each sample was put through five freeze-thaw cycles, kept on ice for 1 h followed by centrifugation to remove calvarial bone and debris, and bone tissue extracts stored at -70°C until required. For TRAP activity detection, 35µL of bone tissue lysates was added to 200 µL of TRAP substrate (50mM sodium acetate, pH 5, 25mM sodium tartrate, 0.4mM $MnCl_2$, 0.4% N,N,-dimethylformamide, 0.2 mg/mL fast red violet, 0.5 mg/mL naphthol AS-MX phosphate), then incubated 3 hours at 37°C, and the absorbance read at 540 nm. Values were normalized for the protein concentration of the calvarial tissue lysates.

Statistical analysis

All values were expressed as mean ± SEM. Unpaired Student's *t* test was used to analyze the differences between two groups, while one- or two-way ANOVA with Bonferroni correction was used to evaluate differences among multiple comparisons. A *P* value of less than 0.05 was considered statistically significant. All representative experiments shown were repeated 3 or more times.

Data availability

The RNA sequencing data from this publication have been deposited to the Gene Expression Omnibus database at accession number GSE212302 (https://www.ncbi.nlm.nih.gov/geo/query/acc.cgi?acc=GSE212302).

Acknowledgements

We thank Dr. Kimberly Stegmaier (Harvard Medical School) for providing the wild-type MtCK1 and metabolic inactive MtCK1^{C316G} mutant expression vectors, S. Meshinchi (University of Michigan Microscopy Core) for assistance in imaging, and C. Whitinger (Michigan Integrative Musculoskeletal Health Core Center) for assistance with bone histomorphometry. This work was supported by grants from the NIH (R01-105068, R01-CA071699 and R01-AR075168), the Breast Cancer Research Foundation and the Margolies Family Discovery Fund for Cancer Research (S.J.W.), the NSFC 81970919, the Fundamental Research Funds for the Central Universities 2042022kf1207 (L.Z.), the DFG TRR305, A03, A04, B01, B02 (T.B.), and P01-CA093900 (E.T.K.). Core support was provided by the National Cancer Institute of the National Institutes of Health under award number P30-AR069620.

Disclosure and Competing Interests Statement

The authors declare that they have no conflict of interest.

References

Almotiri A, Alzahrani H, Menendez-Gonzalez JB, Abdelfattah A, Alotaibi B, Saleh L, Greene A, Georgiou M, Gibbs A, Alsayari A *et al* (2021) Zeb1 modulates hematopoietic stem cell fates required for suppressing acute myeloid leukemia. *J Clin Invest* 131: e129115

Arnett TR, Orriss IR (2018) Metabolic properties of the osteoclast. *Bone* 115: 25-30

Aucher A, Rudnicka D, Davis DM (2013) MicroRNAs transfer from human macrophages to hepato-carcinoma cells and inhibit proliferation. *J Immunol* 191: 6250-6260

Bae S, Lee MJ, Mun SH, Giannopoulou EG, Yong-Gonzalez V, Cross JR, Murata K, Giguere V, van der Meulen M, Park-Min KH (2017) MYC-dependent oxidative metabolism regulates osteoclastogenesis via nuclear receptor ERRalpha. *J Clin Invest* 127: 2555-2568

Bartell SM, Kim HN, Ambrogini E, Han L, Iyer S, Serra Ucer S, Rabinovitch P, Jilka RL, Weinstein RS, Zhao H *et al* (2014) FoxO proteins restrain osteoclastogenesis and bone resorption by attenuating H2O2 accumulation. *Nat Commun* 5: 3773

Bellido T, Delgado-Calle J (2020) Ex Vivo Organ Cultures as Models to Study Bone Biology. *JBMR Plus* 4: 10

Bellon E, Luyten FP, Tylzanowski P (2009) delta-EF1 is a negative regulator of Ihh in the developing growth plate. *J Cell Biol* 187: 685-699

Bian Y, Li W, Kremer DM, Sajjakulnukit P, Li S, Crespo J, Nwosu ZC, Zhang L, Czerwonka A, Pawlowska A *et al* (2020) Cancer SLC43A2 alters T cell methionine metabolism and histone methylation. *Nature* 585: 277-282

Blangy A, Bompard G, Guerit D, Marie P, Maurin J, Morel A, Vives V (2020) The osteoclast cytoskeleton - current understanding and therapeutic perspectives for osteoporosis. *J Cell Sci* 133: jcs244798

Boyle WJ, Simonet WS, Lacey DL (2003) Osteoclast differentiation and activation. *Nature* 423: 337-342

Brabletz S, Lasierra Losada M, Schmalhofer O, Mitschke J, Krebs A, Brabletz T, Stemmler MP (2017) Generation and characterization of mice for conditional inactivation of Zeb1. *Genesis* 55

Cackowski FC, Anderson JL, Patrene KD, Choksi RJ, Shapiro SD, Windle JJ, Blair HC, Roodman GD (2010) Osteoclasts are important for bone angiogenesis. *Blood* 115: 140-149

Callaway DA, Jiang JX (2015) Reactive oxygen species and oxidative stress in osteoclastogenesis, skeletal aging and bone diseases. *J Bone Miner Metab* 33: 359-370

Chang EJ, Ha J, Oerlemans F, Lee YJ, Lee SW, Ryu J, Kim HJ, Lee Y, Kim HM, Choi JY *et al* (2008) Brain-type creatine kinase has a crucial role in osteoclast-mediated bone resorption. *Nat Med* 14: 966-972

Chen W, Gong P, Guo J, Li H, Li R, Xing W, Yang Z, Guan Y (2018) Glycolysis regulates pollen tube polarity via Rho GTPase signaling. *PLoS Genet* 14: e1007373

Compston JE, McClung MR, Leslie WD (2019) Osteoporosis. *Lancet* 393: 364-376

de Barrios O, Sanchez-Moral L, Cortes M, Ninfali C, Profitos-Peleja N, Martinez-Campanario MC, Siles L, Del Campo R, Fernandez-Acenero MJ, Darling DS *et al* (2019) ZEB1 promotes inflammation and progression towards inflammation-driven carcinoma through repression of the DNA repair glycosylase MPG in epithelial cells. *Gut* 68: 2129-2141

Dempster DW, Compston JE, Drezner MK, Glorieux FH, Kanis JA, Malluche H, Meunier PJ, Ott SM, Recker RR, Parfitt AM (2013) Standardized nomenclature, symbols, and units for bone histomorphometry: a 2012 update of the report of the ASBMR Histomorphometry Nomenclature Committee. *J Bone Miner Res* 28: 2-17

Dobin A, Davis CA, Schlesinger F, Drenkow J, Zaleski C, Jha S, Batut P, Chaisson M, Gingeras TR (2013) STAR: ultrafast universal RNA-seq aligner. *Bioinformatics* 29: 15-21

Everts V, Delaisse JM, Korper W, Jansen DC, Tigchelaar-Gutter W, Saftig P, Beertsen W (2002) The bone lining cell: its role in cleaning Howship's lacunae and initiating bone formation. *J Bone Miner Res* 17: 77-90

Feldker N, Ferrazzi F, Schuhwerk H, Widholz SA, Guenther K, Frisch I, Jakob K, Kleemann J, Riegel D, Bonisch U *et al* (2020) Genome-wide cooperation of EMT transcription factor ZEB1 with YAP and AP-1 in breast cancer. *EMBO J* 39: e103209

Feng X, Novack DV, Faccio R, Ory DS, Aya K, Boyer MI, McHugh KP, Ross FP, Teitelbaum SL (2001) A Glanzmann's mutation in beta 3 integrin specifically impairs osteoclast function. *J Clin Invest* 107: 1137-1144

Fenouille N, Bassil CF, Ben-Sahra I, Benajiba L, Alexe G, Ramos A, Pikman Y, Conway AS, Burgess MR, Li Q *et al* (2017) The creatine kinase pathway is a metabolic vulnerability in EVI1-positive acute myeloid leukemia. *Nat Med* 23: 301-313

Ferron M, Settembre C, Shimazu J, Lacombe J, Kato S, Rawlings DJ, Ballabio A, Karsenty G (2013) A RANKL-PKCbeta-TFEB signaling cascade is necessary for lysosomal biogenesis in osteoclasts. *Genes Dev* 27: 955-969

Francou A, Anderson KV (2020) The Epithelial-to-Mesenchymal Transition (EMT) in Development and Cancer. *Annu Rev Cancer Biol* 4: 197-220

Fu R, Lv WC, Xu Y, Gong MY, Chen XJ, Jiang N, Xu Y, Yao QQ, Di L, Lu T *et al* (2020) Endothelial ZEB1 promotes angiogenesis-dependent bone formation and reverses osteoporosis. *Nat Commun* 11: 460

Furter R, Furter-Graves EM, Wallimann T (1993) Creatine kinase: the reactive cysteine is required for synergism but is nonessential for catalysis. *Biochemistry* 32: 7022-7029

Garnero P, Ferreras M, Karsdal MA, Nicamhlaoibh R, Risteli J, Borel O, Qvist P, Delmas PD, Foged NT, Delaisse JM (2003) The type I collagen fragments ICTP and CTX reveal distinct enzymatic pathways of bone collagen degradation. *J Bone Miner Res* 18: 859-867

Ginhoux F, Jung S (2014) Monocytes and macrophages: developmental pathways and tissue homeostasis. *Nat Rev Immunol* 14: 392-404

Goettsch C, Babelova A, Trummer O, Erben RG, Rauner M, Rammelt S, Weissmann N, Weinberger V, Benkhoff S, Kampschulte M *et al* (2013) NADPH oxidase 4 limits bone mass by promoting osteoclastogenesis. *J Clin Invest* 123: 4731-4738

Guo Y, Lu X, Chen Y, Rendon B, Mitchell RA, Cuatrecasas M, Cortes M, Postigo A, Liu Y, Dean DC (2021) Zeb1 induces immune checkpoints to form an immunosuppressive envelope around invading cancer cells. *Sci Adv* 7: eabd7455

Han X, Duan X, Liu Z, Long Y, Liu C, Zhou J, Li N, Qin J, Wang Y (2021) ZEB1 directly inhibits GPX4 transcription contributing to ROS accumulation in breast cancer cells. *Breast Cancer Res Treat* 188: 329-342

Han X, Long Y, Duan X, Liu Z, Hu X, Zhou J, Li N, Wang Y, Qin J (2022) ZEB1 induces ROS generation through directly promoting MCT4 transcription to facilitate breast cancer. *Exp Cell Res* 412: 113044

Holmes T, Brown AW, Suggitt M, Shaw LA, Simpson L, Harrity JPA, Tozer GM, Kanthou C (2020) The influence of hypoxia and energy depletion on the response of endothelial cells to the vascular disrupting agent combretastatin A-4-phosphate. *Sci Rep* 10: 9926

Inada M, Wang Y, Byrne MH, Rahman MU, Miyaura C, Lopez-Otin C, Krane SM (2004) Critical roles for collagenase-3 (Mmp13) in development of growth plate cartilage and in endochondral ossification. *Proc Natl Acad Sci U S A* 101: 17192-17197

Indo Y, Takeshita S, Ishii KA, Hoshii T, Aburatani H, Hirao A, Ikeda K (2013) Metabolic regulation of osteoclast differentiation and function. *J Bone Miner Res* 28: 2392-2399

Izawa T, Rohatgi N, Fukunaga T, Wang QT, Silva MJ, Gardner MJ, McDaniel ML, Abumrad NA, Semenkovich CF, Teitelbaum SL *et al* (2015) ASXL2 Regulates Glucose, Lipid, and Skeletal Homeostasis. *Cell Rep* 11: 1625-1637

Jacome-Galarza CE, Percin GI, Muller JT, Mass E, Lazarov T, Eitler J, Rauner M, Yadav VK, Crozet L, Bohm M *et al* (2019) Developmental origin, functional maintenance and genetic rescue of osteoclasts. *Nature* 568: 541-545

Jiang H, Wei H, Wang H, Wang Z, Li J, Ou Y, Xiao X, Wang W, Chang A, Sun W *et al* (2022) Zeb1-induced metabolic reprogramming of glycolysis is essential for macrophage polarization in breast cancer. *Cell Death Dis* 13: 206

Jiao X, Sherman BT, Huang da W, Stephens R, Baseler MW, Lane HC, Lempicki RA (2012) DAVID-WS: a stateful web service to facilitate gene/protein list analysis. *Bioinformatics* 28: 1805-1806

Kalyanaraman B, Hardy M, Podsiadly R, Cheng G, Zielonka J (2017) Recent developments in detection of superoxide radical anion and hydrogen peroxide: Opportunities, challenges, and implications in redox signaling. *Arch Biochem Biophys* 617: 38-47

Kang IS, Kim C (2016) NADPH oxidase gp91(phox) contributes to RANKL-induced osteoclast differentiation by upregulating NFATc1. *Sci Rep* 6: 38014

Kazak L, Chouchani ET, Jedrychowski MP, Erickson BK, Shinoda K, Cohen P, Vetrivelan R, Lu GZ, Laznik-Bogoslavski D, Hasenfuss SC *et al* (2015) A creatine-driven substrate cycle enhances energy expenditure and thermogenesis in beige fat. *Cell* 163: 643-655

Kazak L, Chouchani ET, Lu GZ, Jedrychowski MP, Bare CJ, Mina AI, Kumari M, Zhang S, Vuckovic I, Laznik-Bogoslavski D *et al* (2017) Genetic Depletion of Adipocyte Creatine Metabolism Inhibits Diet-Induced Thermogenesis and Drives Obesity. *Cell Metab* 26: 660-671

Kazak L, Cohen P (2020) Creatine metabolism: energy homeostasis, immunity and cancer biology. *Nat Rev Endocrinol* 16: 421-436

Khoury BM, Bigelow EM, Smith LM, Schlecht SH, Scheller EL, Andarawis-Puri N, Jepsen KJ (2015) The use of nano-computed tomography to enhance musculoskeletal research. *Connect Tissue Res* 56: 106-119

Kim MS, Yang YM, Son A, Tian YS, Lee SI, Kang SW, Muallem S, Shin DM (2010) RANKL-mediated reactive oxygen species pathway that induces long lasting Ca2+ oscillations essential for osteoclastogenesis. *J Biol Chem* 285: 6913-6921

Krebs AM, Mitschke J, Lasierra Losada M, Schmalhofer O, Boerries M, Busch H, Boettcher M, Mougiakakos D, Reichardt W, Bronsert P *et al* (2017) The EMT-activator Zeb1 is a key factor for cell plasticity and promotes metastasis in pancreatic cancer. *Nat Cell Biol* 19: 518-529

Kurmi K, Hitosugi S, Yu J, Boakye-Agyeman F, Wiese EK, Larson TR, Dai Q, Machida YJ, Lou Z, Wang L *et al* (2018) Tyrosine Phosphorylation of Mitochondrial Creatine Kinase 1 Enhances a Druggable Tumor Energy Shuttle Pathway. *Cell Metab* 28: 833-847

Kurotaki D, Yoshida H, Tamura T (2020) Epigenetic and transcriptional regulation of osteoclast differentiation. *Bone* 138: 115471

Larsen JE, Nathan V, Osborne JK, Farrow RK, Deb D, Sullivan JP, Dospoy PD, Augustyn A, Hight SK, Sato M *et al* (2016) ZEB1 drives epithelial-to-mesenchymal transition in lung cancer. *J Clin Invest* 126: 3219-3235

Lee NK, Choi YG, Baik JY, Han SY, Jeong DW, Bae YS, Kim N, Lee SY (2005) A crucial role for reactive oxygen species in RANKL-induced osteoclast differentiation. *Blood* 106: 852-859

Lemma S, Sboarina M, Porporato PE, Zini N, Sonveaux P, Di Pompo G, Baldini N, Avnet S (2016) Energy metabolism in osteoclast formation and activity. *Int J Biochem Cell Biol* 79: 168-180

Li B, Lee WC, Song C, Ye L, Abel ED, Long F (2020) Both aerobic glycolysis and mitochondrial respiration are required for osteoclast differentiation. *FASEB J* 34: 11058-11067

Liao Y, Smyth GK, Shi W (2014) featureCounts: an efficient general purpose program for assigning sequence reads to genomic features. *Bioinformatics* 30: 923-930

Ling W, Krager K, Richardson KK, Warren AD, Ponte F, Aykin-Burns N, Manolagas SC, Almeida M, Kim HN (2021) Mitochondrial Sirt3 contributes to the bone loss caused by aging or estrogen deficiency. *JCI Insight* 6: e146728

Little AC, Kovalenko I, Goo LE, Hong HS, Kerk SA, Yates JA, Purohit V, Lombard DB, Merajver SD, Lyssiotis CA (2020) High-content fluorescence imaging with the metabolic flux assay reveals insights into mitochondrial properties and functions. *Commun Biol* 3: 271

Liu Y, El-Naggar S, Darling DS, Higashi Y, Dean DC (2008) Zeb1 links epithelial-mesenchymal transition and cellular senescence. *Development* 135: 579-588

Love MI, Huber W, Anders S (2014) Moderated estimation of fold change and dispersion for RNA-seq data with DESeq2. *Genome Biol* 15: 550

Macosko EZ, Basu A, Satija R, Nemesh J, Shekhar K, Goldman M, Tirosh I, Bialas AR, Kamitaki N, Martersteck EM *et al* (2015) Highly Parallel Genome-wide Expression Profiling of Individual Cells Using Nanoliter Droplets. *Cell* 161: 1202-1214

Masin M, Vazquez J, Rossi S, Groeneveld S, Samson N, Schwalie PC, Deplancke B, Frawley LE, Gouttenoire J, Moradpour D *et al* (2014) GLUT3 is induced during epithelial-mesenchymal transition and promotes tumor cell proliferation in non-small cell lung cancer. *Cancer Metab* 2: 11

Mathow D, Chessa F, Rabionet M, Kaden S, Jennemann R, Sandhoff R, Grone HJ, Feuerborn A (2015) Zeb1 affects epithelial cell adhesion by diverting glycosphingolipid metabolism. *EMBO Rep* 16: 321-331

Morel AP, Ginestier C, Pommier RM, Cabaud O, Ruiz E, Wicinski J, Devouassoux-Shisheboran M, Combaret V, Finetti P, Chassot C *et al* (2017) A stemness-related ZEB1-MSRB3 axis governs cellular pliancy and breast cancer genome stability. *Nat Med* 23: 568-578

Murata K, Fang C, Terao C, Giannopoulou EG, Lee YJ, Lee MJ, Mun SH, Bae S, Qiao Y, Yuan R *et al* (2017) Hypoxia-Sensitive COMMD1 Integrates Signaling and Cellular Metabolism in Human Macrophages and Suppresses Osteoclastogenesis. *Immunity* 47: 66-79

Murphy MP, Bayir H, Belousov V, Chang CJ, Davies KJA, Davies MJ, Dick TP, Finkel T, Forman HJ, Janssen-Heininger Y *et al* (2022) Guidelines for measuring reactive oxygen species and oxidative damage in cells and in vivo. *Nat Metab* 4: 651-662

Nagai Y, Osawa K, Fukushima H, Tamura Y, Aoki K, Ohya K, Yasuda H, Hikiji H, Takahashi M, Seta Y *et al* (2013) p130Cas, Crk-associated substrate, plays important roles in osteoclastic bone resorption. *J Bone Miner Res* 28: 2449-2462

Nakahira K, Haspel JA, Rathinam VA, Lee SJ, Dolinay T, Lam HC, Englert JA, Rabinovitch M, Cernadas M, Kim HP *et al* (2011) Autophagy proteins regulate innate immune responses by inhibiting the release of mitochondrial DNA mediated by the NALP3 inflammasome. *Nat Immunol* 12: 222-230

Nakano S, Inoue K, Xu C, Deng Z, Syrovatkina V, Vitone G, Zhao L, Huang XY, Zhao B (2019) G-protein Galpha13 functions as a cytoskeletal and mitochondrial regulator to restrain osteoclast function. *Sci Rep* 9: 4236

Nieto MA, Huang RY, Jackson RA, Thiery JP (2016) Emt: 2016. *Cell* 166: 21-45

Nishikawa K, Iwamoto Y, Kobayashi Y, Katsuoka F, Kawaguchi S, Tsujita T, Nakamura T, Kato S, Yamamoto M, Takayanagi H *et al* (2015) DNA methyltransferase 3a regulates osteoclast differentiation by coupling to an S-adenosylmethionine-producing metabolic pathway. *Nat Med* 21: 281-287

Postigo AA, Dean DC (1999) Independent repressor domains in ZEB regulate muscle and T-cell differentiation. *Mol Cell Biol* 19: 7961-7971

Postigo AA, Dean DC (2000) Differential expression and function of members of the zfh-1 family of zinc finger/homeodomain repressors. *Proc Natl Acad Sci U S A* 97: 6391-6396

Rahbani JF, Roesler A, Hussain MF, Samborska B, Dykstra CB, Tsai L, Jedrychowski MP, Vergnes L, Reue K, Spiegelman BM *et al* (2021) Creatine kinase B controls futile creatine cycling in thermogenic fat. *Nature* 590: 480-485

Raynaud-Messina B, Bracq L, Dupont M, Souriant S, Usmani SM, Proag A, Pingris K, Soldan V, Thibault C, Capilla F *et al* (2018) Bone degradation machinery of osteoclasts: An HIV-1 target that contributes to bone loss. *Proc Natl Acad Sci U S A* 115: E2556-E2565

Rosmaninho P, Mukusch S, Piscopo V, Teixeira V, Raposo AA, Warta R, Bennewitz R, Tang Y, Herold-Mende C, Stifani S *et al* (2018) Zeb1 potentiates genome-wide gene transcription with Lef1 to promote glioblastoma cell invasion. *EMBO J* 37: e97115

Ruh M, Stemmler MP, Frisch I, Fuchs K, van Roey R, Kleemann J, Roas M, Schuhwerk H, Eccles RL, Agaimy A *et al* (2021) The EMT transcription factor ZEB1 blocks osteoblastic differentiation in bone development and osteosarcoma. *J Pathol* 254: 199-211

Sanjay A, Houghton A, Neff L, DiDomenico E, Bardelay C, Antoine E, Levy J, Gailit J, Bowtell D, Horne WC *et al* (2001) Cbl associates with Pyk2 and Src to regulate Src kinase activity, alpha(v)beta(3) integrin-mediated signaling, cell adhesion, and osteoclast motility. *J Cell Biol* 152: 181-195

Schlattner U, Tokarska-Schlattner M, Wallimann T (2006) Mitochondrial creatine kinase in human health and disease. *Biochim Biophys Acta* 1762: 164-180

Schroder K (2019) NADPH oxidases in bone homeostasis and osteoporosis. *Free Radic Biol Med* 132: 67-72

Shang X, Marchioni F, Evelyn CR, Sipes N, Zhou X, Seibel W, Wortman M, Zheng Y (2013) Small-molecule inhibitors targeting G-protein-coupled Rho guanine nucleotide exchange factors. *Proc Natl Acad Sci U S A* 110: 3155-3160

Sims NA, Martin TJ (2020) Osteoclasts Provide Coupling Signals to Osteoblast Lineage Cells Through Multiple Mechanisms. *Annu Rev Physiol* 82: 507-529

Srivastava AK, Bhattacharyya S, Castillo G, Miyakoshi N, Mohan S, Baylink DJ (2000) Development and evaluation of C-telopeptide enzyme-linked immunoassay for measurement of bone resorption in mouse serum. *Bone* 27: 529-533

Stemmler MP, Eccles RL, Brabletz S, Brabletz T (2019) Non-redundant functions of EMT transcription factors. *Nat Cell Biol* 21: 102-112

Takagi T, Moribe H, Kondoh H, Higashi Y (1998) DeltaEF1, a zinc finger and homeodomain transcription factor, is required for skeleton patterning in multiple lineages. *Development* 125: 21-31

Takayanagi H (2007) Osteoimmunology: shared mechanisms and crosstalk between the immune and bone systems. *Nat Rev Immunol* 7: 292-304

Tang Y, Feinberg T, Keller ET, Li XY, Weiss SJ (2016) Snail/Slug binding interactions with YAP/TAZ control skeletal stem cell self-renewal and differentiation. *Nat Cell Biol* 18: 917-929

Tang Y, Wu X, Lei W, Pang L, Wan C, Shi Z, Zhao L, Nagy TR, Peng X, Hu J *et al* (2009) TGF-beta1-induced migration of bone mesenchymal stem cells couples bone resorption with formation. *Nat Med* 15: 757-765

Teitelbaum SL (2011) The osteoclast and its unique cytoskeleton. *Ann N Y Acad Sci* 1240: 14-17

Teitelbaum SL, Ross FP (2003) Genetic regulation of osteoclast development and function. *Nat Rev Genet* 4: 638-649

Touaitahuata H, Blangy A, Vives V (2014) Modulation of osteoclast differentiation and bone resorption by Rho GTPases. *Small GTPases* 5: e28119

Tsukasaki M, Huynh NC, Okamoto K, Muro R, Terashima A, Kurikawa Y, Komatsu N, Pluemsakunthai W, Nitta T, Abe T *et al* (2020) Stepwise cell fate decision pathways during osteoclastogenesis at single-cell resolution. *Nat Metab* 2: 1382-1390

Uehara S, Udagawa N, Mukai H, Ishihara A, Maeda K, Yamashita T, Murakami K, Nishita M, Nakamura T, Kato S *et al* (2017) Protein kinase N3 promotes bone resorption by osteoclasts in response to Wnt5a-Ror2 signaling. *Sci Signal* 10: eaan0023

Vandewalle C, Van Roy F, Berx G (2009) The role of the ZEB family of transcription factors in development and disease. *Cell Mol Life Sci* 66: 773-787

Wallimann T, Tokarska-Schlattner M, Schlattner U (2011) The creatine kinase system and pleiotropic effects of creatine. *Amino Acids* 40: 1271-1296

Wallimann T, Wyss M, Brdiczka D, Nicolay K, Eppenberger HM (1992) Intracellular compartmentation, structure and function of creatine kinase isoenzymes in tissues with high and fluctuating energy demands: the 'phosphocreatine circuit' for cellular energy homeostasis. *Biochem J* 281 (Pt1): 21-40

Weivoda MM, Oursler MJ (2014) The Roles of Small GTPases in Osteoclast Biology. *Orthop Muscular Syst* 3: 1000161

Wu D, Harrison DL, Szasz T, Yeh CF, Shentu TP, Meliton A, Huang RT, Zhou Z, Mutlu GM, Huang J *et al* (2021) Single-cell metabolic imaging reveals a SLC2A3-dependent glycolytic burst in motile endothelial cells. *Nat Metab* 3: 714-727

Wu M, Chen W, Lu Y, Zhu G, Hao L, Li YP (2017) Galpha13 negatively controls osteoclastogenesis through inhibition of the Akt-GSK3beta-NFATc1 signalling pathway. *Nat Commun* 8: 13700

Xu WY, Hu QS, Qin Y, Zhang B, Liu WS, Ni QX, Xu J, Yu XJ (2018) Zinc finger E-box-binding homeobox 1 mediates aerobic glycolysis via suppression of sirtuin 3 in pancreatic cancer. *World J Gastroenterol* 24: 4893-4905

Yahara Y, Barrientos T, Tang YJ, Puviindran V, Nadesan P, Zhang H, Gibson JR, Gregory SG, Diao Y, Xiang Y *et al* (2020) Erythromyeloid progenitors give rise to a population of osteoclasts that contribute to bone homeostasis and repair. *Nat Cell Biol* 22: 49-59

Zaidi M (2007) Skeletal remodeling in health and disease. *Nat Med* 13: 791-801

Zeng R, Faccio R, Novack DV (2015) Alternative NF-kappaB Regulates RANKL-Induced Osteoclast Differentiation and Mitochondrial Biogenesis via Independent Mechanisms. *J Bone Miner Res* 30: 2287-2299

Zhang C, Liu J, Liang Y, Wu R, Zhao Y, Hong X, Lin M, Yu H, Liu L, Levine AJ *et al* (2013) Tumour-associated mutant p53 drives the Warburg effect. *Nat Commun* 4: 2935

Zhang J, Wang J, Xing H, Li Q, Zhao Q, Li J (2016) Down-regulation of FBP1 by ZEB1-mediated repression confers to growth and invasion in lung cancer cells. *Mol Cell Biochem* 411: 331-340

Zhang K, Zhao H, Sheng Y, Chen X, Xu P, Wang J, Ji Z, He Y, Gao WQ, Zhu HH (2022) Zeb1 sustains hematopoietic stem cell functions by suppressing mitofusin-2-mediated mitochondrial fusion. *Cell Death Dis* 13: 735

Zhang Y, Rohatgi N, Veis DJ, Schilling J, Teitelbaum SL, Zou W (2018) PGC1beta Organizes the Osteoclast Cytoskeleton by Mitochondrial Biogenesis and Activation. *J Bone Miner Res* 33: 1114-1125

Zhao X, Lin S, Li H, Si S, Wang Z (2021) Myeloperoxidase Controls Bone Turnover by Suppressing Osteoclast Differentiation Through Modulating Reactive Oxygen Species Level. *J Bone Miner Res* 36: 591-603

Zhou B, Jin W (2020) Visualization of Single Cell RNA-Seq Data Using t-SNE in R. *Methods Mol Biol* 2117: 159-167

Zhou Y, Lin F, Wan T, Chen A, Wang H, Jiang B, Zhao W, Liao S, Wang S, Li G *et al* (2021) ZEB1 enhances Warburg effect to facilitate tumorigenesis and metastasis of HCC by transcriptionally activating PFKM. *Theranostics* 11: 5926-5938

Zhu L, Tang Y, Li XY, Keller ET, Yang J, Cho JS, Feinberg TY, Weiss SJ (2020) Osteoclast-mediated bone resorption is controlled by a compensatory network of secreted and membrane-tethered metalloproteinases. *Sci Transl Med* 12: eaaw6143

Zhu X, Yan F, Liu L, Huang Q (2022) ZEB1 regulates bone metabolism in osteoporotic rats through inducing POLDIP2 transcription. *J Orthop Surg Res* 17: 423

Zou W, Kitaura H, Reeve J, Long F, Tybulewicz VL, Shattil SJ, Ginsberg MH, Ross FP, Teitelbaum SL (2007) Syk, c-Src, the alphavbeta3 integrin, and ITAM immunoreceptors, in concert, regulate osteoclastic bone resorption. *J Cell Biol* 176: 877-888

Zou W, Rohatgi N, Chen TH, Schilling J, Abu-Amer Y, Teitelbaum SL (2016) PPAR-gamma regulates pharmacological but not physiological or pathological osteoclast formation. *Nat Med* 22: 1203-1205

Figure Legends

Figure 1. Mouse osteoclasts express Zeb1 *in vitro* and *in vivo*.

A DAVID gene ontology (GO) analysis of differentially upregulated transcripts during BMDM-osteoclast transition generated from wild-type mice identified an enrichment in DNA-binding TF activity (arrow; $n = 3$).

B Unexpected expression of Zeb1 (arrow) among the top 20 differentially upregulated genes retrieved from DAVID GO biological process “DNA-binding TF activity” during wild-type BMDM-osteoclast transition ($n = 3$).

C Relative mRNA expression of *Zeb1*, *Acp5,* and *Ctsk* during the differentiation from BMDMs to osteoclasts in culture ($n = 3$).

D Western blot of Zeb1, c-Src, and Ctsk expression in BMDMs and mature osteoclasts ($n = 3$).

E 3D reconstruction of Zeb1 (red), TRAP (green), and F-actin (cyan) immunofluorescent staining of osteoclasts differentiated from wild-type BMDMs. Scale bar, 20 µm.

F Zeb1 (red) and TRAP (green) immunofluorescence of a femur section including the growth plate (GP) and metaphysis from a wild-type mouse. The multinucleated cells associated with the surface of the bone marrow cavity (BM cavity) that are shown in the red box are further enlarged in the panels to the right. Scale bar, 10 µm.

Data information: Bars and error bars represent mean ± SEM. Data are representative of at least 3 independent experiments with biological replicates. Data were analyzed using unpaired Student’s *t* test (C). $^{**}P < 0.01$.

Source data are available online for this figure.

Figure 2. *Zeb1* conditional knockout mice are osteopenic with heightened bone resorptive activity *in vivo*.

A Representative nanoCT of sagittal sections of femurs with 3D reconstruction of the distal femur trabeculae of 3-month-old wild-type and *Zeb1*$^{\Delta M/\Delta M}$ male mice are shown. The genotype of *Zeb1*$^{+/+}$, *Zeb1*$^{f/+}$, *Zeb*$^{f/f}$ mice is defined as “wild-type” control. Scale bar, 500 µm.

B Quantification of BV/TV, Tb.Th, Tb.N, and Tb.Sp as determined by nanoCT in 3-month-old wild-type and *Zeb1*$^{\Delta M/\Delta M}$ male mice (*n* = 8).

C H&E and TRAP staining of the distal femurs of 3-month-old male wild-type and *Zeb1*$^{\Delta M/\Delta M}$ mice. Scale bar, 200 µm.

D Quantification of osteoclast number per bone surface (N.Oc/BS) and eroded surface per bone surface (ES/BS), as well as serum CTX-I and OCN levels in 3-month-old wild-type and *Zeb1*$^{\Delta M/\Delta M}$ male mice are shown (*n* = 6).

E Golden’s trichrome staining illuminating howship’s lacunae (arrow) of the distal femurs of 3-month-old male wild-type and *Zeb1*$^{\Delta M/\Delta M}$ mice were performed along with double-calcein bone labeling and confocal imaging to assess bone formation. Scale bar, 10 µm.

F Quantification of MAR and BFR as assessed in 3-month-old male wild-type and *Zeb1*$^{\Delta M/\Delta M}$ mice (*n* = 6).

Data information: Bars and error bars represent mean ± SEM. Data are representative of at least 3 independent experiments with biological replicates. Data were analyzed using unpaired Student’s *t* test (B, D, F). ns, not significant; $^{**}P < 0.01$.

Figure 3. Enhanced sealing zone formation and bone resorbing activity of *Zeb1*-knockout osteoclasts *in vitro*.

A BMDMs were isolated from wild-type or *Zeb1*$^{\Delta M/\Delta M}$ mice and cultured atop plastic substrata with M-CSF and RANKL for 5 d, stained with TRAP, and the number of TRAP$^+$ MNCs determined (*n* = 6). Scale bar, 500 µm.

B Zeb1, NFATc1, c-Fos, c-Src, β3 integrin, Mmp9, Mmp14, and Ctsk expression as assessed by Western blot in wild-type and *Zeb1*$^{\Delta M/\Delta M}$ BMDMs during osteoclast differentiation (*n* = 3).

C, D After a 6-day culture period, wild-type or *Zeb1*$^{\Delta M/\Delta M}$ osteoclasts were removed from bone slices, resorption pits visualized by WGA-DAB staining (C), and resorption pit area quantified (D; *n* = 6). Scale bar, 100 µm.

E, F Resorption pits were 3D reconstructed by reflective confocal laser scanning microscope (RCLSM) (F) in tandem with quantification of resorption pit depth (E; *n* = 6). Color bar, pit depth.

G Supernatant CTX-I determined by ELISA (*n* = 6).

H, I After a 6-day culture atop bone slice, phalloidin staining (red) was performed in wild-type versus *Zeb1*$^{\Delta M/\Delta M}$ osteoclasts (I), and actin ring area per cell quantified (H). Scale bar, 20 µm.

Data information: Bars and error bars represent mean ± SEM. Data are representative of at least 3 independent experiments with biological replicates. Data were analyzed using unpaired Student's *t* test (A, D, E, G, H). ns, not significant; **P* < 0.05, ***P* < 0.01.

Source data are available online for this figure.

Figure 4. Zeb1 represses MtCK1 expression and tunes the phosphocreatine energy shuttle in osteoclasts.

A Volcano plot showing significantly enriched and depleted mRNAs in *Zeb1*$^{\Delta M/\Delta M}$ osteoclasts versus wild-type osteoclasts (*n* = 3).

B The top 10 most highly upregulated and downregulated transcripts in *Zeb1*$^{\Delta M/\Delta M}$ osteoclasts as compared with wild-type osteoclasts are presented (*n* = 3; color bar, relative expression value). C DAVID gene ontology (GO) analysis of differentially expressed genes from *Zeb1*-deleted versus wild-type osteoclasts.

D Mitochondrial creatine kinase activity of wild-type and *Zeb1*$^{\Delta M/\Delta M}$ BMDMs and osteoclasts cultured atop plastic substrata (*n* = 3).

E Relative mRNA expression of *Ckmt1* in BMDMs and osteoclasts generated from wild-type or *Zeb1*$^{\Delta M/\Delta M}$ mice.

F MtCK1, Ckb, VDAC, and Tomm20 expression as assessed by Western blot in BMDMs and osteoclasts generated from wild-type or *Zeb1*$^{\Delta M/\Delta M}$ mice (*n* = 3).

G MtCK1 and Ckb expression in the mitochondrial fraction as assessed by Western blot in BMDMs and osteoclasts generated from wild-type or *Zeb1*$^{\Delta M/\Delta M}$ mice (*n* = 3).

H MtCK1 (green) immunofluorescence of wild-type and *Zeb1*$^{\Delta M/\Delta M}$ osteoclasts. Scale bar, 20 μm.

I Schematic of mouse *Ckmt1* promoter region indicating locations of E-box (red) and Z-box (blue) sequences that represent putative Zeb1 binding sites.

J Luciferase activity was monitored in RAW 264.7 cells co-transfected with a mock or ZEB1 expression vector in combination with a *Ckmt1* promoter reporter construct (*n* = 3).

K qPCR analysis of ChIP using anti-Zeb1 antibody at the *Ckmt1* promoter region in mature osteoclasts generated from wild-type or *Zeb1*$^{\Delta M/\Delta M}$ mice (*n* = 3).

Data information: Bars and error bars represent mean ± SEM. Data are representative of at least 3 independent experiments with biological replicates. Data were analyzed using two-way ANOVA with Bonferroni correction (D, E, J, K). ns, not significant; *$P < 0.05$, **$P < 0.01$.

Source data are available online for this figure.

Figure 5. *Zeb1* depletion increases mitochondrial respiration and ATP production in osteoclasts.

A Phosphocreatine (PCr) and creatine (Cr) level, as well as PCr/Cr ratio of wild-type or *Zeb1*$^{\Delta M/\Delta M}$ osteoclasts cultured atop plastic substrata as determined by LC/MS analysis (*n* = 3).

B, C Oxygen consumption rate (OCR) profile plot (B) and mitochondrial function parameters (C) analyzed by XF Cell Mito Stress Assay in osteoclasts from wild-type or *Zeb1*$^{\Delta M/\Delta M}$ mice after sequential treatment of compounds modulating mitochondrial function (*n* = 4).

D Ultrastructural appearance of mitochondria in BMDMs and osteoclasts generated from wild-type or *Zeb1*$^{\Delta M/\Delta M}$ mice. Scale bar, 100 nm.

E ATP levels of BMDMs and osteoclasts generated from wild-type or *Zeb1*$^{\Delta M/\Delta M}$ mice (*n* = 3).

F RhoA activity of wild-type and *Zeb1*$^{\Delta M/\Delta M}$ osteoclasts cultured on plastic (*n* = 6).

Data information: Bars and error bars represent mean ± SEM. Data are representative of at least 3 independent experiments with biological replicates. Data were analyzed using unpaired Student's *t* test (A, C, F) or two-way ANOVA with Bonferroni correction (E). ns, not significant; $^{**}P < 0.01$.

Figure 6. Mitochondrial creatine kinase activity drives mitochondrial bioenergetics.

A A schematic diagram of the mock vector, wild-type human MtCK1, and the metabolic inactive MtCK1^{C316G} mutant expression vector.

B Wild-type BMDMs were transduced with wild-type human MtCK1, differentiated into osteoclasts, and stained with HA (green), MtCK1 (red), and Tomm20 (cyan). Scale bar, 20 μm.

C Wild-type BMDMs were transduced with either a mock vector, wild-type human MtCK1, or a catalytically-inactive MtCK1^{C316G} mutant expression vector, differentiated into osteoclasts, and cell lysates collected for MtCK1, Ckb, Tomm20, VDAC, Zeb1, c-Src, and Ctsk immunoblotting (*n* = 3).

D Mitochondrial creatine kinase activity of mock vector-, MtCK1-, or MtCK1^{C316G}-transduced wild-type osteoclasts cultured on plastic (*n* = 3).

E PCr/Cr ratio of mock vector-, MtCK1-, or MtCK1^{C316G}-transduced wild-type osteoclasts cultured on plastic substrata as determined by LC/MS analysis (*n* = 3).

F ATP levels of mock vector-, MtCK1-, or MtCK1^{C316G}-transduced wild-type osteoclasts (*n* = 3).

G Wild-type BMDMs were transduced with lentiviral vectors expressing wild-type MtCK1, a catalytically-inactive MtCK1^{C316G} mutant, or a mock control and differentiated into osteoclasts, and RhoA activity assessed (*n* = 6).

H, I OCR profile plot (H) and mitochondrial function parameters (I) analyzed by XF Cell Mito Stress Assay in mock vector-, MtCK1-, or MtCK1^{C316G}-transduced wild-type osteoclasts after sequential treatment of compounds modulating mitochondrial function (*n* = 4).

J, K Mock vector-, MtCK1-, or MtCK1^{C316G}-transduced wild-type pre-osteoclasts were cultured atop bone slices for 3 days, stained with phalloidin (red). Osteoclasts were removed and resorption pits visualized by WGA-DAB staining (J). The actin ring area per cell and resorption pit area were quantified (K; *n* = 6). Scale bar, upper 20 μm, lower 100 μm.

Data information: Bars and error bars represent mean ± SEM. Data are representative of at least 3 independent experiments with biological replicates. Data were analyzed using one-way ANOVA with Bonferroni correction (D-G, I, K). ns, not significant; *$P < 0.05$, **$P < 0.01$.

Source data are available online for this figure.

Figure 7. The Zeb1/MtCK1 axis controls sealing zone formation and osteoclast activity.

A, B Human monocyte-derived macrophages (hMDMs) were transfected with either sh*CTRL* or siRNA targeting *ZEB1*, differentiated into osteoclasts, and relative mRNA expression of *CKMT1* (A) and mitochondrial creatine kinase activity determined (B; *n* = 3).

C PCr/Cr ratio of osteoclasts differentiated from non-targeting si*CTRL*- or si*ZEB1*-transfected hMDMs cultured atop plastic substrata as determined by LC/MS analysis (*n* = 3).

D, E ATP levels (D) and RhoA activity (E) of osteoclasts differentiated from non-targeting si*CTRL*- or si*ZEB1*-transfected hMDMs.

F Mitochondrial function parameters analyzed by XF Cell Mito Stress Assay in non-targeting si*CTRL*- or si*ZEB1*-transfected osteoclasts after sequential treatment of compounds modulating mitochondrial function (*n* = 4).

G, H si*CTRL*- or si*ZEB1*-transfected human osteoclasts were cultured atop bone slices for 6 days and stained with phalloidin (red). Osteoclasts were removed and resorption pits visualized by WGA-DAB staining (G). Scale bar, upper 20 µm, lower 100 µm. The actin ring area per cell, resorption pit area, and the number of TRAP$^+$ MNCs were quantified (H; *n* = 6).

I-L Calvaria isolated from wild-type and $Zeb1^{\Delta M/\Delta M}$ mice were cultured in the presence or absence of 200 µM cyclocreatine, and stained for phalloidin (red) and Vpp3 (green) (I). Scale bar, 10 µm. The TRAP activity of whole cell lysates, actin ring area per cell, and supernatant CTX-I were quantified (J-L; *n* = 6).

Data information: Bars and error bars represent mean ± SEM. Data are representative of at least 3 independent experiments with biological replicates. Data were analyzed using one-way ANOVA with Bonferroni correction (A-F, H, J-L). ns, not significant; *$P < 0.05$, **$P < 0.01$.

EV Figure Legends

Figure EV1. Osteoclasts upregulate Zeb1 mouse and human osteoclasts.

A *t*-Distributed stochastic neighbour embedding (*t*-SNE) plots of cells from E14.5 embryos identified 19 clusters including osteoclasts (Data ref: Yahara *et al.*, 2020).

B Violin plots showing mRNA expression value of *Zeb1* in each cell cluster from E14.5 embryos *in vivo*, with the x axis number representing cluster identity (Data ref: Yahara *et al.*, 2020).

C Relative mRNA expression of *ZEB1* and *CTSK* in human monocyte-derived macrophages (hMDMs) and mature human osteoclasts (hOC; $n = 3$).

D ZEB1, β3 INTEGRIN, and CTSK protein expression as assessed by Western blot were determined in hMDMs and mature hOCs.

E ZEB1 (red) and F-actin (green) staining of human osteoclasts differentiated from hMDM. Scale bar, 20 µm.

Data information: Bars and error bars represent mean ± SEM. Data are representative of at least 3 independent experiments with biological replicates. Data were analyzed using unpaired Student’s *t* test (C). $^{**}P < 0.01$.

Source data are available online for this figure.

Figure EV2. *Zeb1*$^{\Delta M/\Delta M}$ mice exhibit decreased bone mass in femur and lumbar vertebrae.

A Schematic of breeding strategy to generate myeloid-selective *Zeb1* knockout mice (*Csf1r-Cre/Zeb1*$^{f/f}$; *Zeb1*$^{\Delta M/\Delta}$).

B Quantification of BV/TV, Tb.Th, Tb.N, and Tb.Sp as determined by nanoCT in 3-month-old wild-type and *Zeb1*$^{\Delta M/\Delta M}$ female mice ($n = 6$).

C Quantification of cortical thickness (Ct.Th) as determined by nanoCT in femurs of 3 month-old wild-type and *Zeb1*$^{\Delta M/\Delta M}$ male mice ($n = 8$).

D Representative nanoCT of L3 vertebrae sections of 3-month-old wild-type and *Zeb1*$^{\Delta M/\Delta M}$ male mice are shown. Scale bar, 500 μm.

E Quantification of BV/TV, Tb.Th, Tb.N, and Tb.Sp as determined by nanoCT in L3 vertebrae of 3 month-old wild-type and *Zeb1*$^{\Delta M/\Delta M}$ male mice ($n = 6$). **$P < 0.01$.

Data information: Bars and error bars represent mean ± SEM. Data are representative of at least 3 independent experiments with biological replicates. Data were analyzed using unpaired Student's *t* test (B, C, E). **$P < 0.01$.

Figure EV3. Zeb1 negatively regulates MtCK1 expression in mouse and human osteoclasts.

A Relative expression of creatine metabolism-related transcripts during wild-type BMDM-osteoclast transition as retrieved from gene profiling dataset (Zhu *et al.*, 2020).

B Relative mRNA expression of *Slc6a8*, *Slc6a12, Gatm*, *Gamt, MtCK2, Ckb*, and *Ckm* in BMDMs and osteoclasts generated from wild-type or *Zeb1*$^{\Delta M/\Delta M}$ mice (*n* = 3).

C An empty control vector (EV)-transduced wild-type BMDMs, and EV- or ZEB1-transduced *Zeb1*$^{\Delta M/\Delta M}$ BMDMs, were differentiated into osteoclasts, and cell lysates collected for MtCK1, Ckb, VDAC, c-Src, and Ctsk immunoblotting (*n* = 3).

D MtCK1 (green) and TRAP (red) immunofluorescence of a femur section from wild-type and *Zeb1*$^{\Delta M/\Delta M}$ mice. GP, growth plate. Scale bar, 20 µm.

E, F hMDMs were transfected with either a non-targeting control siRNA (si*CTRL*) or siRNA targeting *ZEB1*, differentiated into osteoclasts, and cell lysates collected for ZEB1, MtCK1, CKB, c-SRC, and CTSK immunoblotting (E) and quantified (F; *n* = 3).

G, H MtCK1 (red) immunofluorescence of si*CTRL-* or *siZEB1-transfected* human osteoclasts (H) and quantified (G; *n* = 3). Scale bar, 20 µm.

Data information: Bars and error bars represent mean ± SEM. Data are representative of at least 3 independent experiments with biological replicates. Data were analyzed using two-way ANOVA with Bonferroni correction (B) and one-way ANOVA with Bonferroni correction (F, G). ns, not significant; **P* < 0.05, ***P* < 0.01.

Source data are available online for this figure.

Figure EV4. Zeb1-dependent mitochondrial creatine kinase activity drives osteoclast activation.

A Wild-type osteoclasts were cultured with exogenous 2 μM phosphocreatine and RhoA activity determined (*n* = 6).

B-D TRAP (red), WGA-DAB and phalloidin staining (red) of wild-type osteoclasts cultured atop bone slices in the presence of exogenous 2 μM phosphocreatine (D). Scale bar, upper and middle 100 μm, lower 20 μm. The number of TRAP$^+$ MNCs, resorption pit area, and actin ring area per cell were quantified (B and C; *n* = 6).

E Scrambled shRNA control vector (sh*Ctrl*)-transduced wild-type BMDMs, and sh*Ctrl*- or sh*Ckmt1*-transduced *Zeb1*$^{\Delta M/\Delta M}$ BMDMs, were differentiated into osteoclasts, and cell lysates collected for MtCK1, Ckb, Tomm20, VDAC, Zeb1, c-Src, and Ctsk immunoblotting (*n* = 3).

F Mitochondrial creatine kinase activity of sh*Ctrl*-transduced wild-type osteoclasts, and sh*Ctrl*- or sh*Ckmt1*-transduced *Zeb1*$^{\Delta M/\Delta M}$ osteoclasts cultured on plastic (*n* = 3).

G PCr/Cr ratio of scrambled sh*Ctrl*-transduced wild-type osteoclasts, and sh*Ctrl*- or sh*Ckmt1*-transduced *Zeb1*$^{\Delta M/\Delta M}$ osteoclasts cultured on plastic as determined by LC/MS analysis (*n* = 3).

H, I ATP levels (H) and RhoA activity (I) of sh*Ctrl*-transduced wild-type osteoclasts, and sh*Ctrl*- or sh*Ckmt1*-transduced *Zeb1*$^{\Delta M/\Delta M}$ osteoclasts (*n* = 3).

J, K sh*Ctrl*-transduced wild-type pre-osteoclasts, and sh*Ctrl*- or sh*Ckmt1*-transduced *Zeb1*$^{\Delta M/\Delta M}$ pre-osteoclasts were cultured atop bone slices for 3 days, stained with phalloidin (red). Osteoclasts were removed and resorption pits visualized by WGA-DAB staining (K). Scale bar, upper 20 μm, lower 100 μm. The actin ring area per cell and resorption pit area were quantified (J).

Data information: Bars and error bars represent mean ± SEM. Data are representative of at least 3 independent experiments with biological replicates. Data were analyzed using unpaired Student's *t* test (A-C) or one-way ANOVA with Bonferroni correction (F-J). ns, not significant; **P* < 0.05, ***P* < 0.01.

Source data are available online for this figure.

Figure EV5. MtCK1 regulates human osteoclast mitochondrial bioenergetics and bone resorption.

A hMDMs were transfected with either non-targeting si*CTRL* or siRNA targeting *CKMT1*, differentiated into osteoclasts, and cell lysates collected for MtCK1, CKB, ZEB1, c-SRC, and CTSK immunoblotting (*n* = 3).

B Mitochondrial creatine kinase activity of si*CTRL*- or si*CKMT1*-transfected osteoclasts cultured on plastic (*n* = 3).

C Phosphocreatine/creatine (PCr/Cr) ratio of si*CTRL*- or si*CKMT1*-transfected osteoclasts cultured on plastic as determined by LC/MS analysis (*n* = 3).

D, E ATP levels (D) and RhoA activity (E) of si*CTRL*- or si*CKMT1*-transfected osteoclasts.

F Mitochondrial function parameters analyzed by XF Cell Mito Stress Assay in si*CTRL*- or si*CKMT1*-transfected osteoclasts after sequential treatment of compounds modulating mitochondrial function (*n* = 4).

G, H si*CTRL*- or si*CKMT1*-transfected human osteoclasts were cultured atop bone slices for 3 days, stained with phalloidin (red). Osteoclasts were removed and resorption pits visualized by WGA-DAB staining (G). Scale bar, upper 20 µm, middle and lower 100 µm. The actin ring area per cell and resorption pit area were quantified (H; *n* = 6).

I TRAP, resorption pits visualized with WGA-DAB staining, and phalloidin staining in wild-type osteoclasts treated with vehicle, and $Zeb1^{\Delta M/\Delta M}$ osteoclasts treated with vehicle or 200 µM cyclocreatine cultured on bone slices with the number of $TRAP^{+}$ MNCs, resorption pit area, and actin ring area per cell quantified (*n* = 6).

Data information: Bars and error bars represent mean ± SEM. Data are representative of at least 3 independent experiments with biological replicates. Data were analyzed using one-way ANOVA with Bonferroni correction (B-F, H, I). ns, not significant; $^{*}P < 0.05$, $^{**}P < 0.01$.

Source data are available online for this figure.

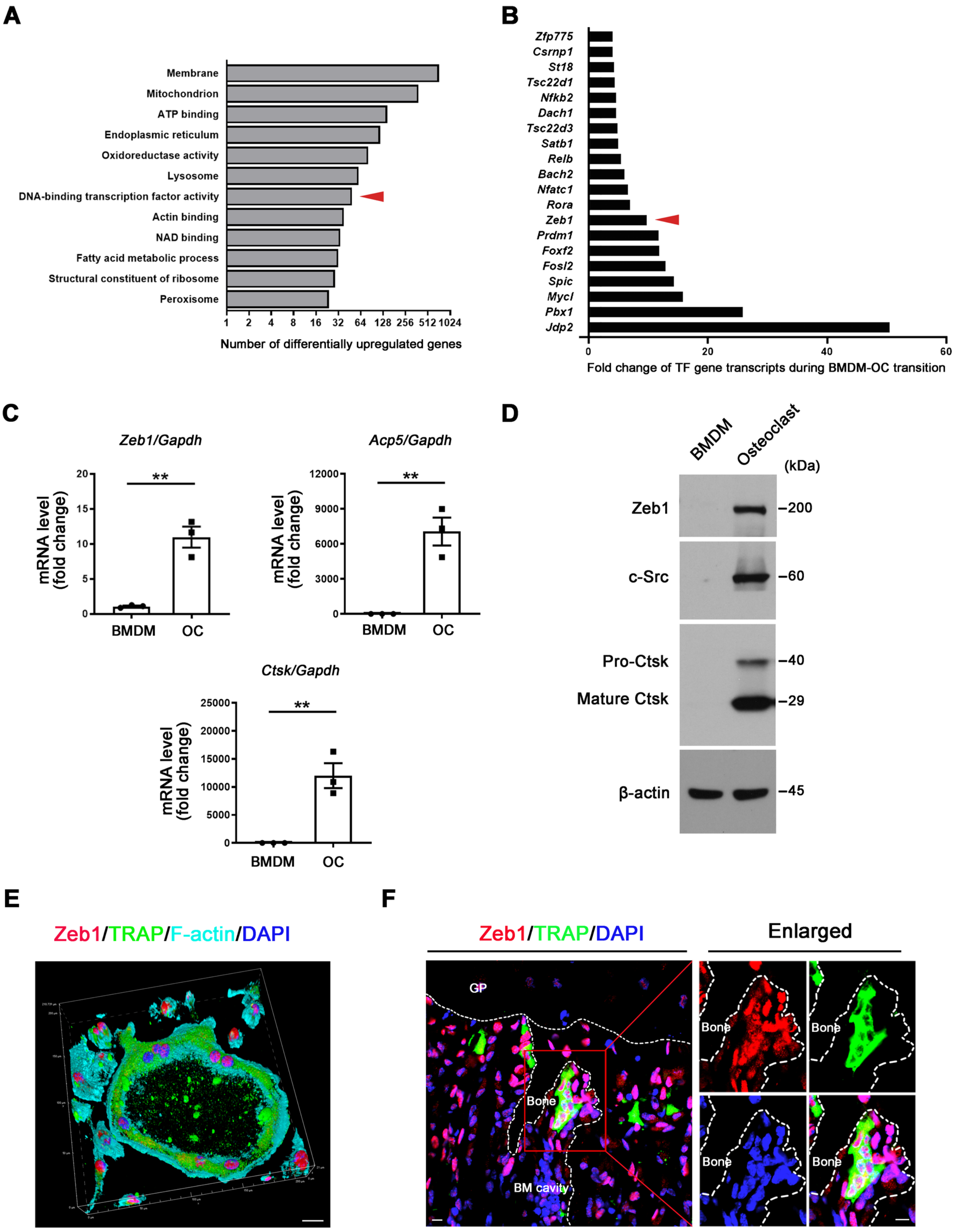

EMBJ_2565_EMBOJ2022111148R2_Fig1.tif

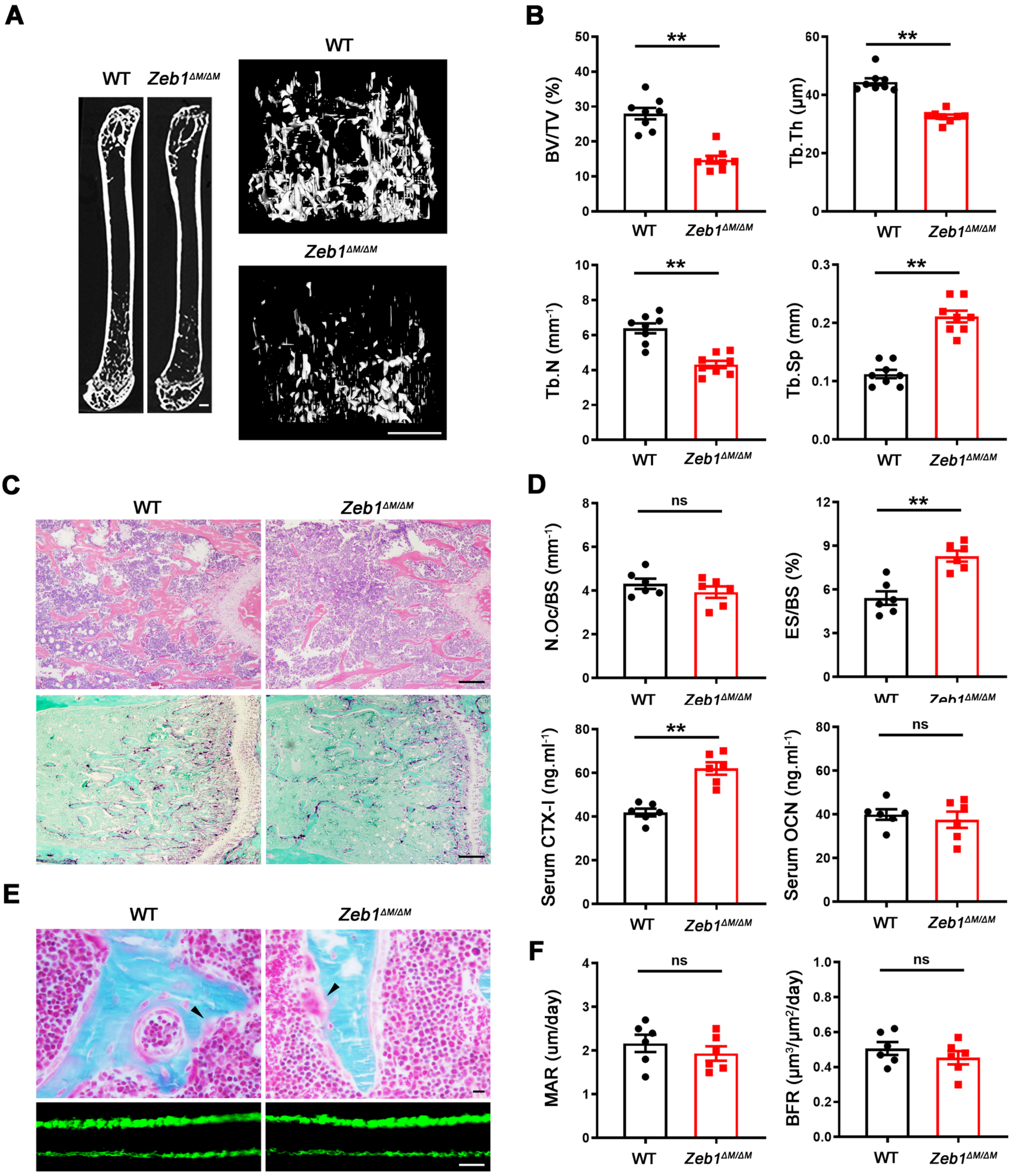

EMBJ_2565_EMBOJ2022111148R2_Fig2.tif

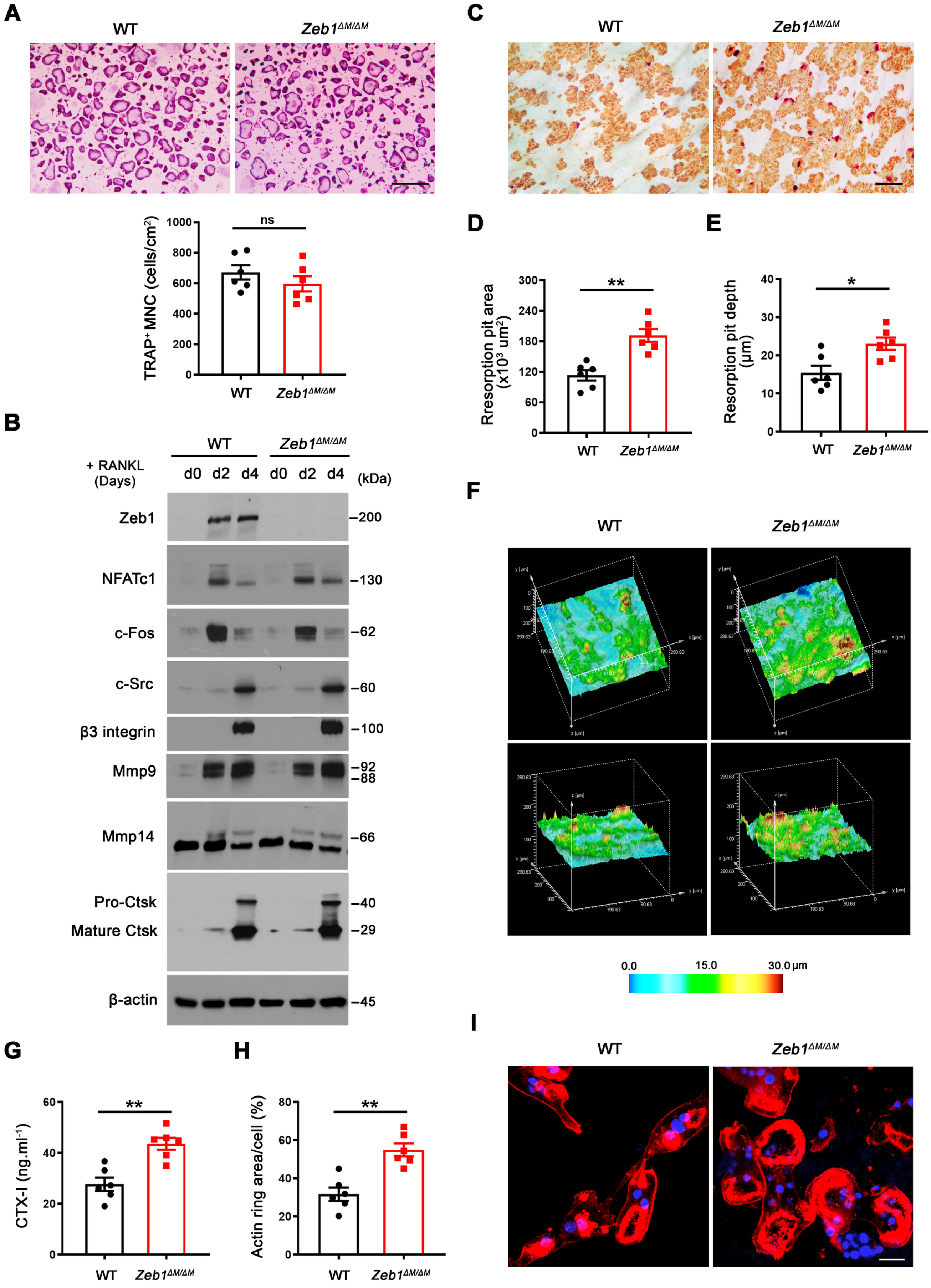

EMBJ_2565_EMBOJ2022111148R2_Fig3.tif

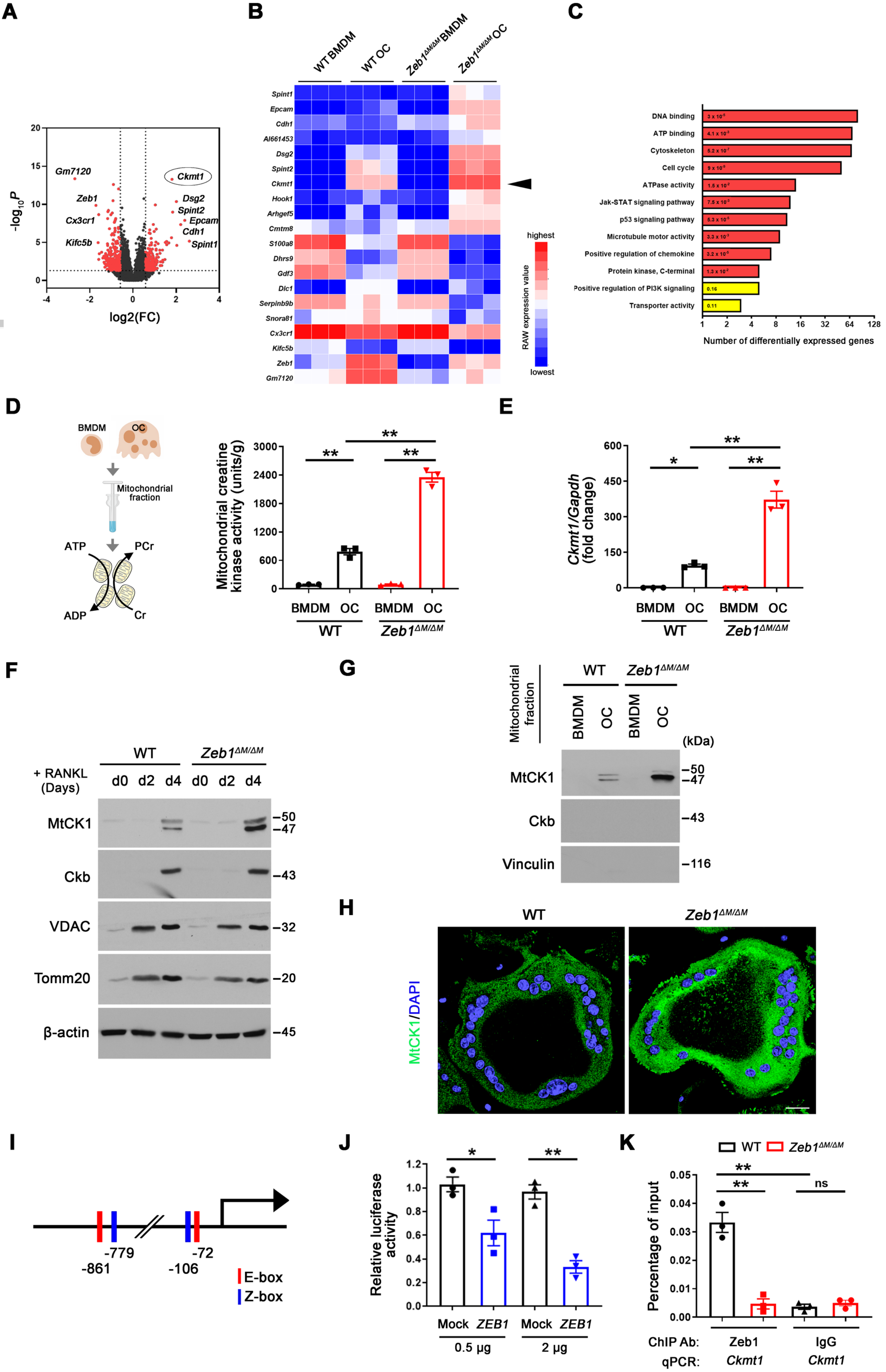

EMBJ_2565_EMBOJ2022111148R2_Fig4.tif

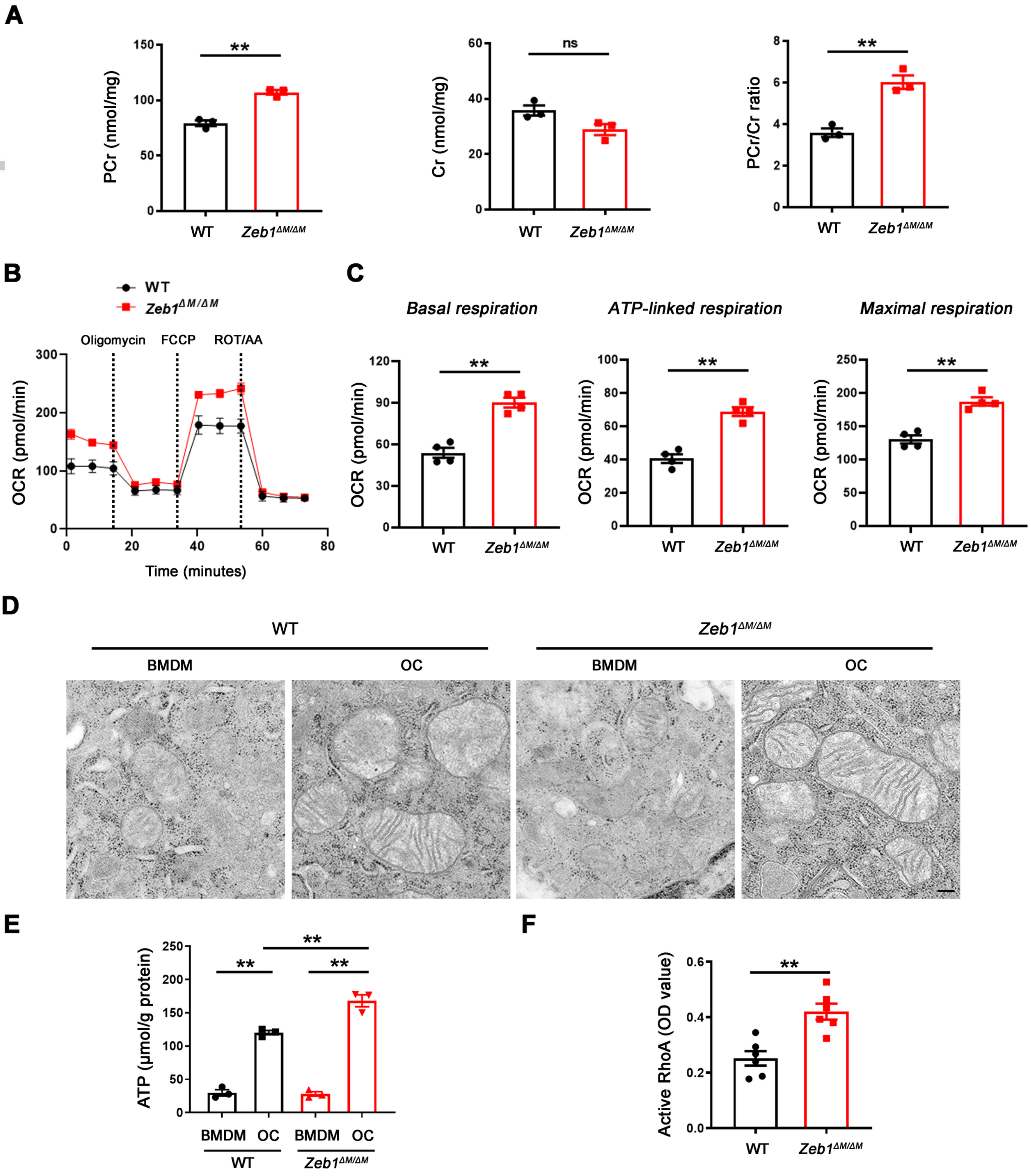

EMBJ_2565_EMBOJ2022111148R2_Fig5.tif

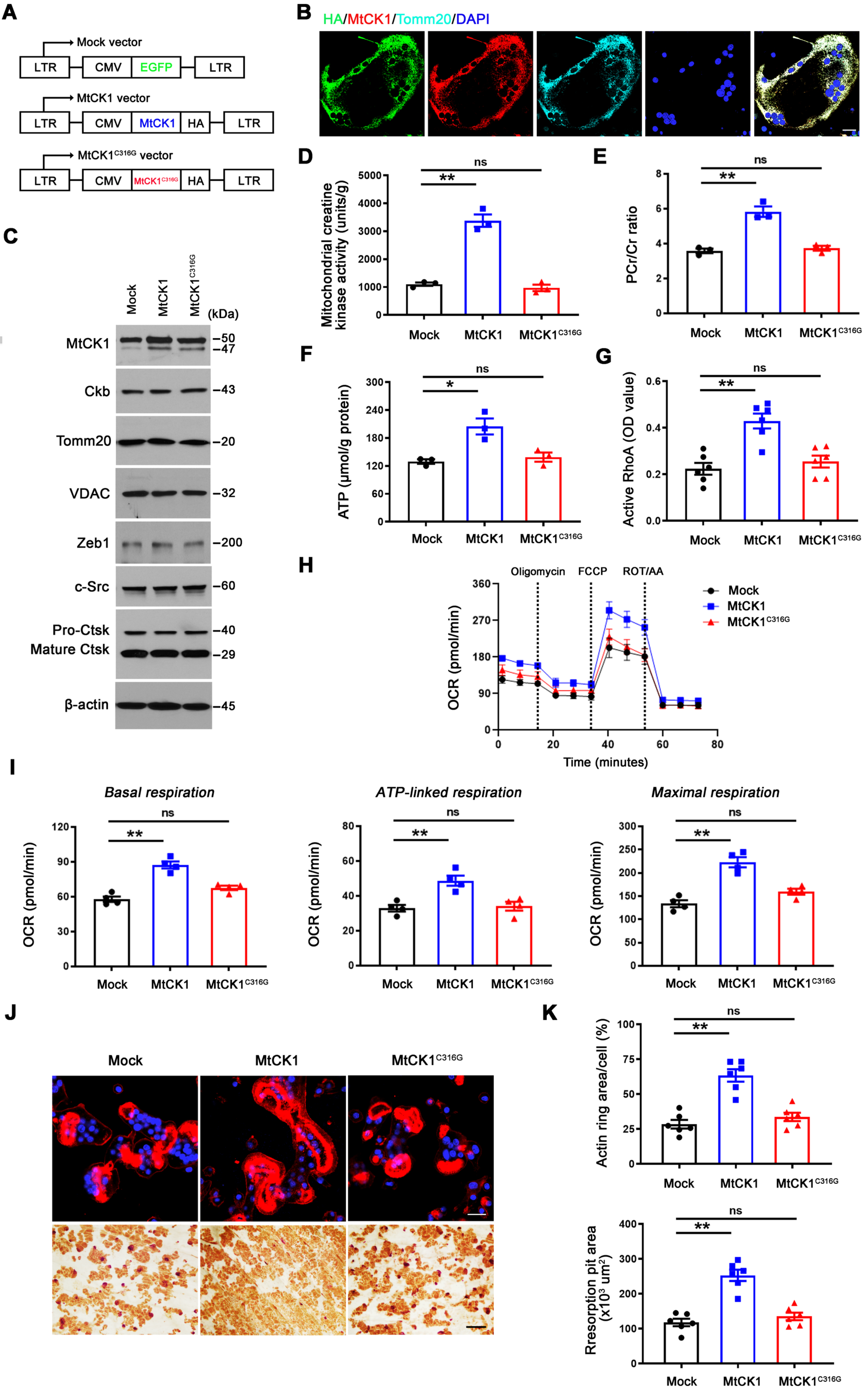
A
Mock vector
LTR
CMV
EGFP
LTR
MtCK1 vector
LTR
CMV
MtCK1
HA
LTR
MtCK1^{C316G} vector
LTR
CMV
MtCK1^{C316G}
HA
LTR
B
HA/MtCK1/Tomm20/DAPI
C
Mock
MtCK1
MtCK1^{C316G}
(kDa)
MtCK1
50
47
Ckb
43
Tomm20
20
VDAC
32
Zeb1
200
c-Src
60
Pro-Ctsk
40
Mature Ctsk
29
β-actin
45
D
Mitochondrial creatine kinase activity (units/g)
5000
4000
3000
2000
1000
0
ns
**
Mock
MtCK1
MtCK1^{C316G}
E
PCr/Cr ratio
8
6
4
2
0
ns
**
Mock
MtCK1
MtCK1^{C316G}
F
ATP (μmol/g protein)
300
240
180
120
60
0
ns
*
Mock
MtCK1
MtCK1^{C316G}
G
Active RhoA (OD value)
0.6
0.4
0.2
0.0
ns
**
Mock
MtCK1
MtCK1^{C316G}
H
Oligomycin
FCCP
ROT/AA
OCR (pmol/min)
360
270
180
90
0
0
20
40
60
80
Time (minutes)
Mock
MtCK1
MtCK1^{C316G}
I
Basal respiration
OCR (pmol/min)
120
90
60
30
0
ns
**
Mock
MtCK1
MtCK1^{C316G}
ATP-linked respiration
OCR (pmol/min)
80
60
40
20
0
ns
**
Mock
MtCK1
MtCK1^{C316G}
Maximal respiration
OCR (pmol/min)
300
250
200
150
100
50
0
ns
**
Mock
MtCK1
MtCK1^{C316G}
J
Mock
MtCK1
MtCK1^{C316G}
K
Actin ring area/cell (%)
100
75
50
25
0
ns
**
Mock
MtCK1
MtCK1^{C316G}
Rresorption pit area (x10^3 um^2)
400
300
200
100
0
ns
**
Mock
MtCK1
MtCK1^{C316G}

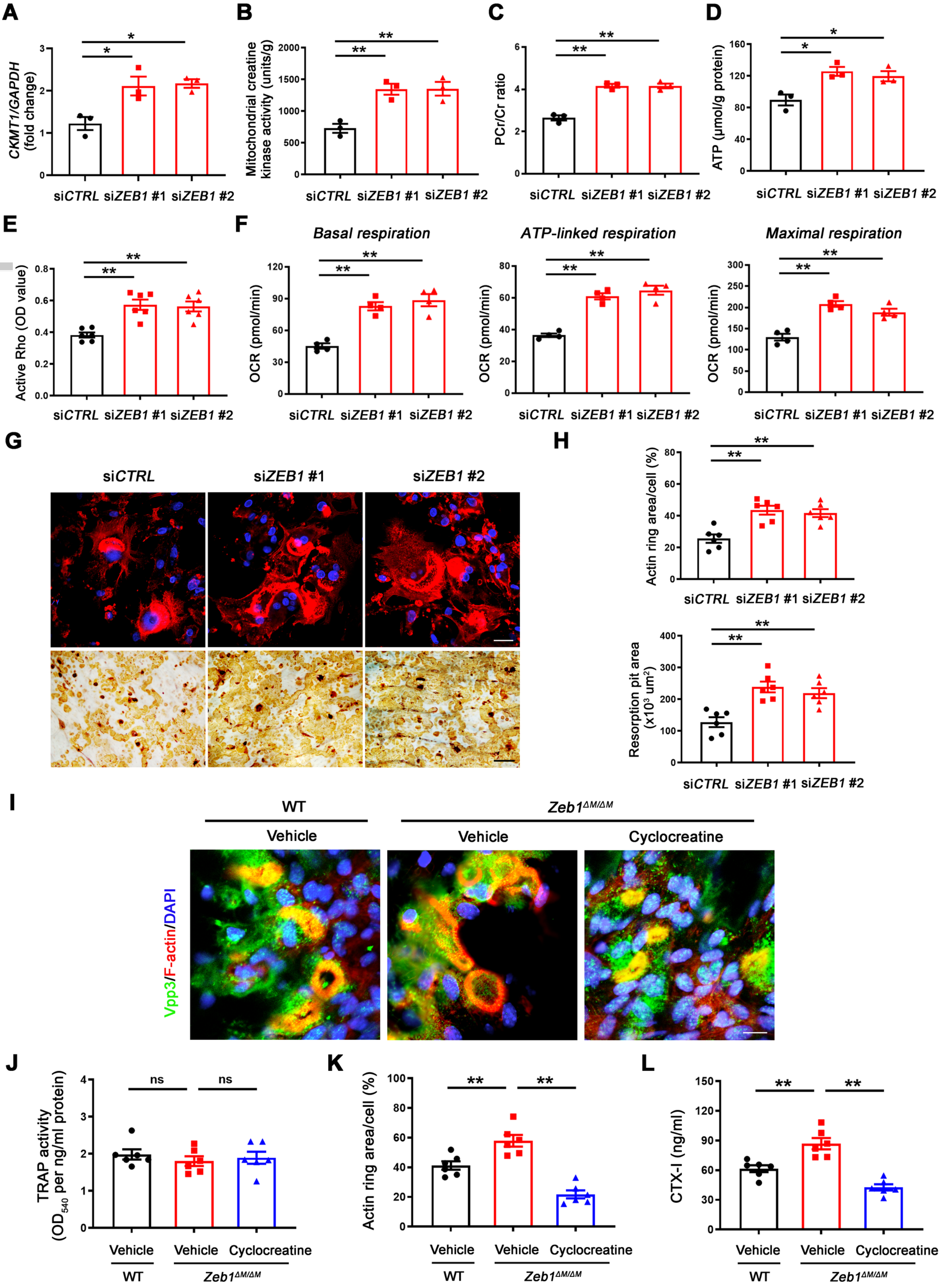

EMBJ_2565_EMBOJ2022111148R2_Fig7.tif

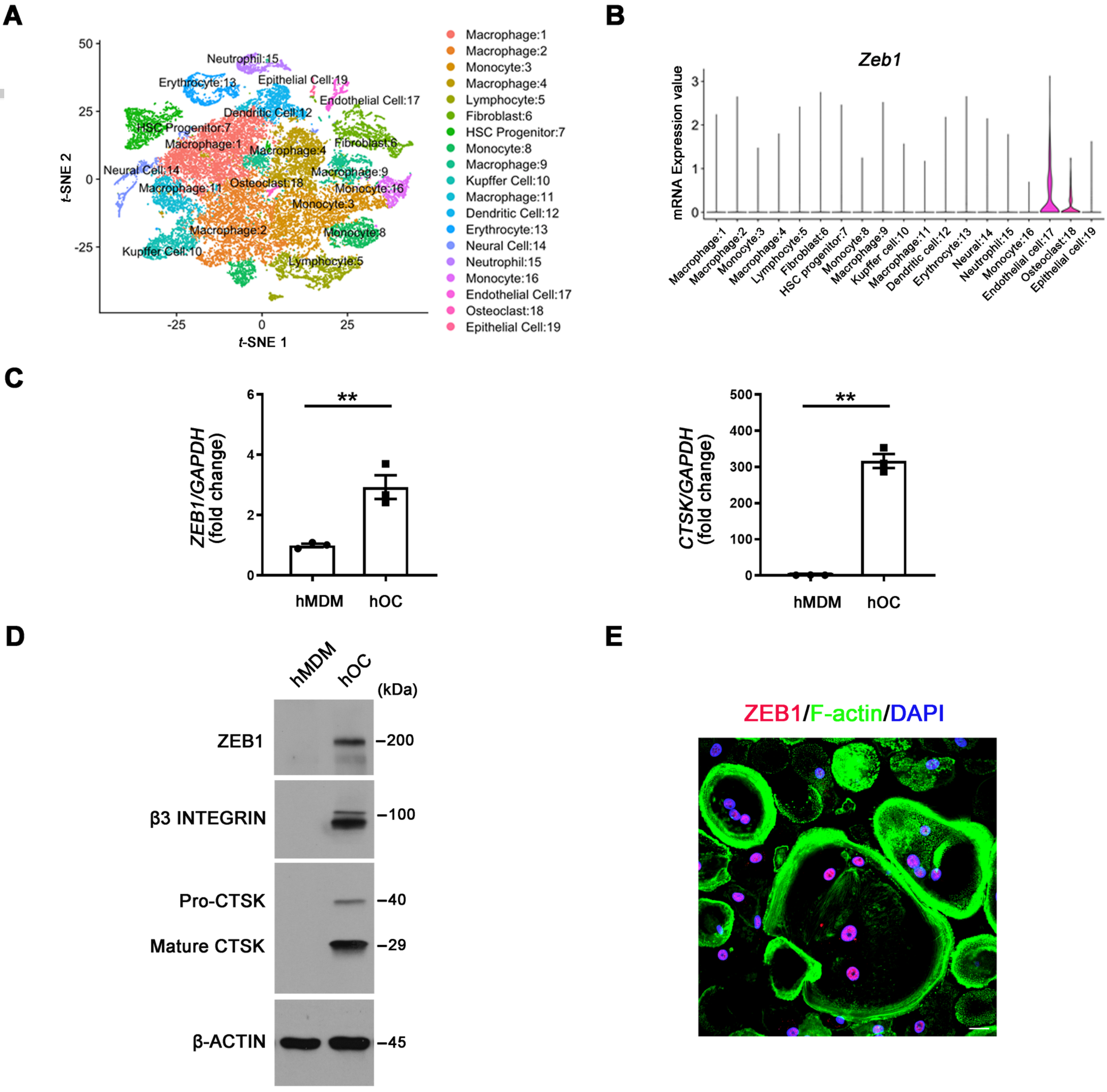

EMBJ_2565_EMBOJ2022111148R2_FigEV1.tif

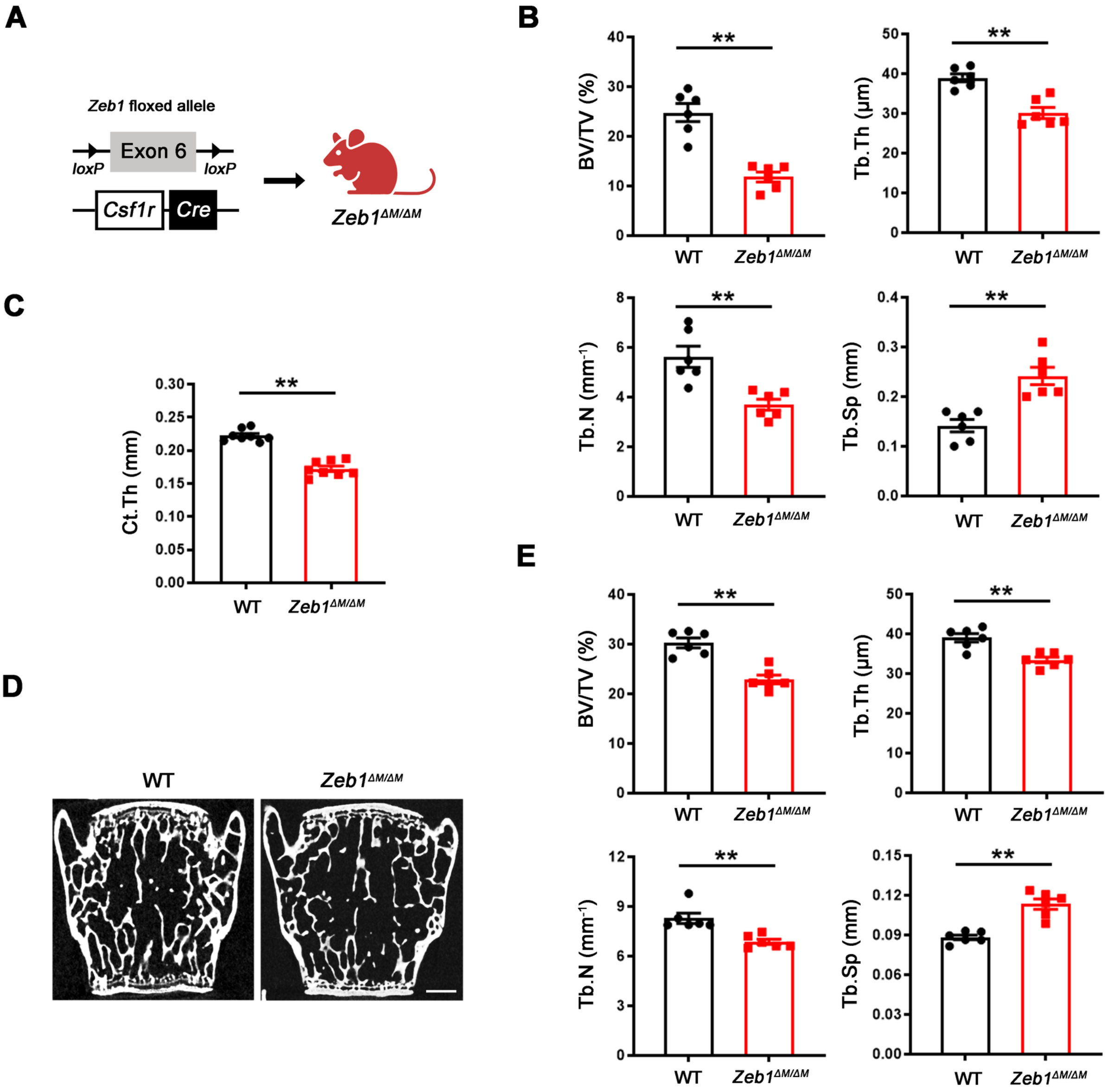

EMBJ_2565_EMBOJ2022111148R2_FigEV2.tif

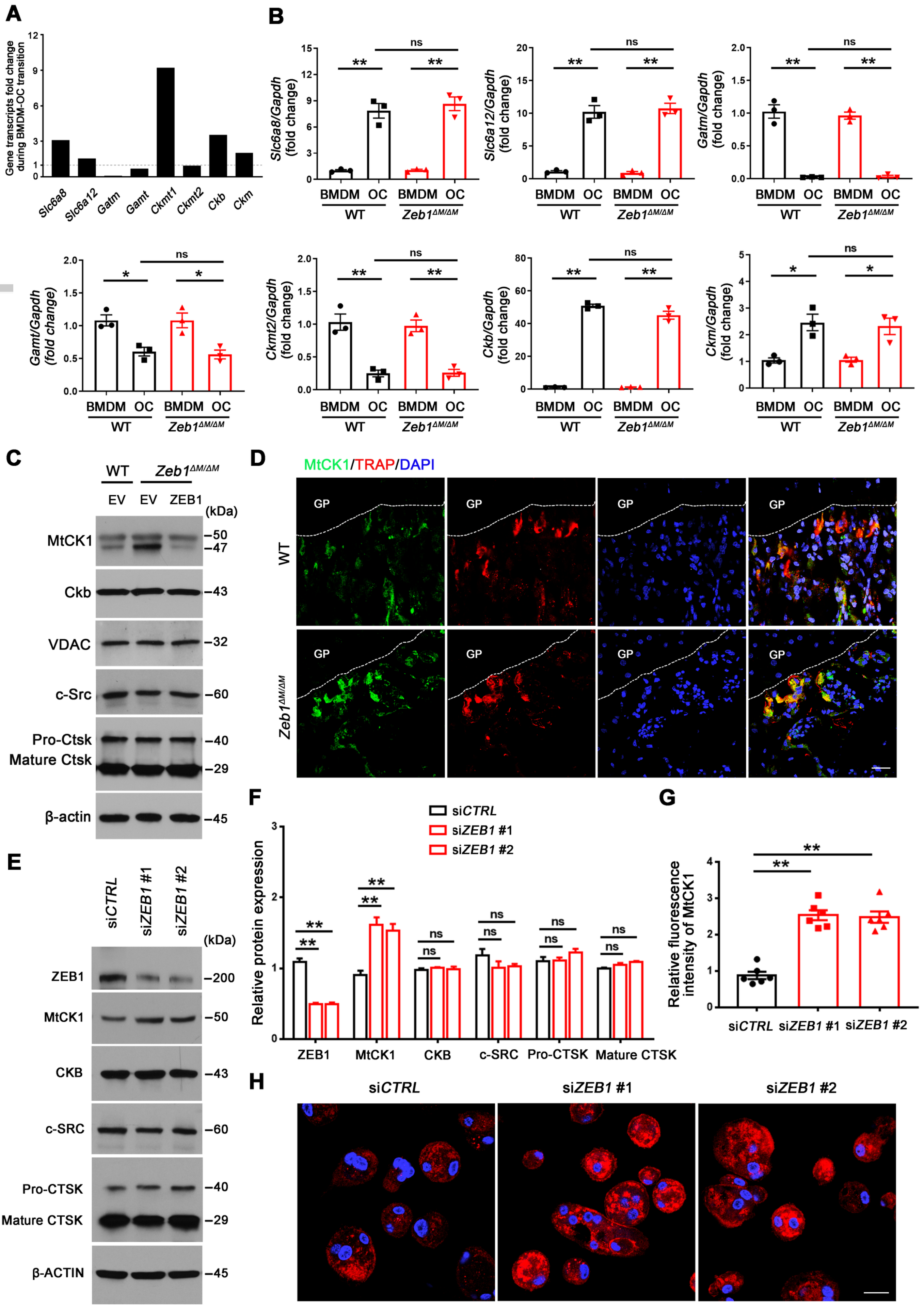

EMBJ_2565_EMBOJ2022111148R2_FigEV3.tif

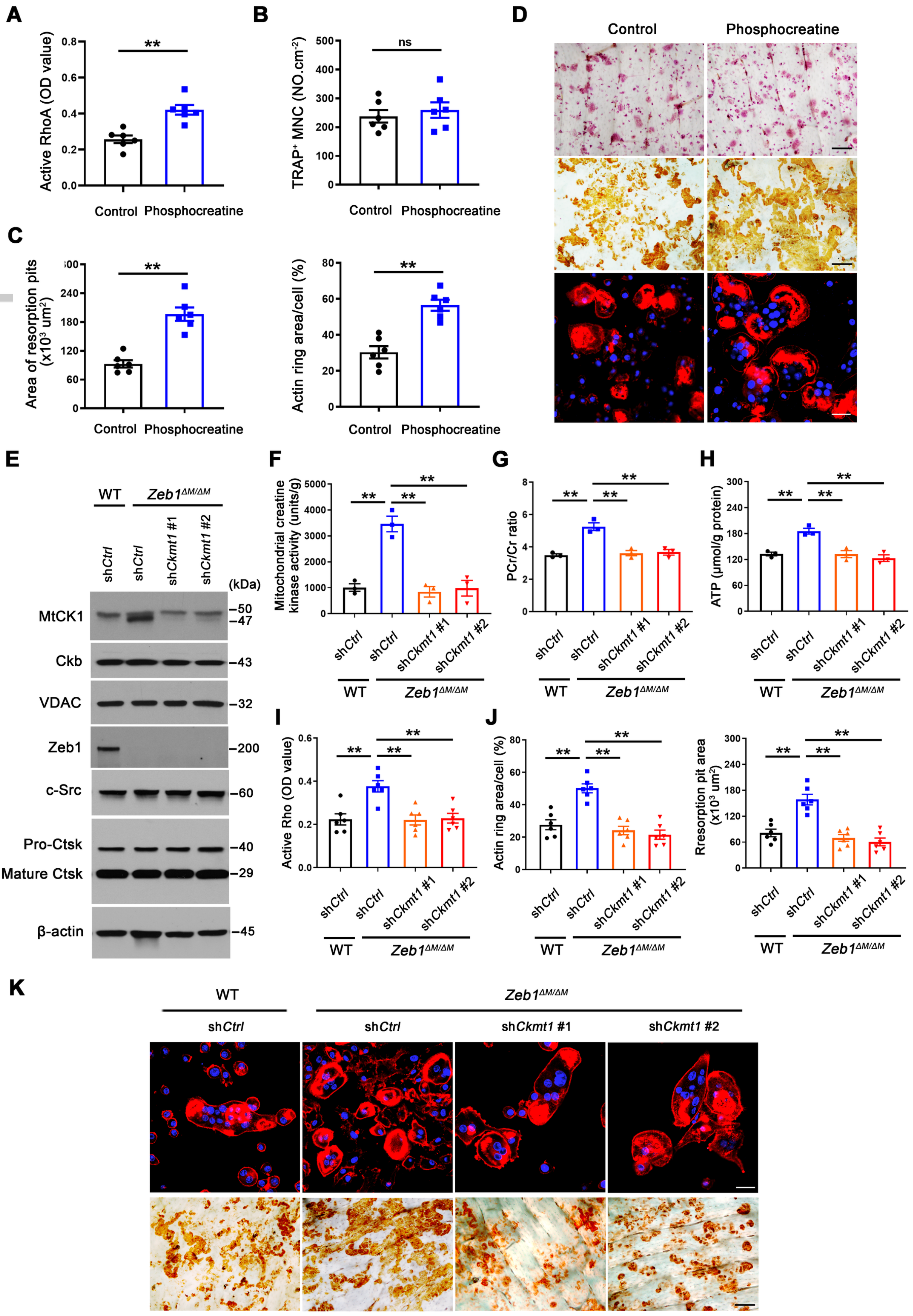

EMBJ_2565_EMBOJ2022111148R2_FigEV4.tif

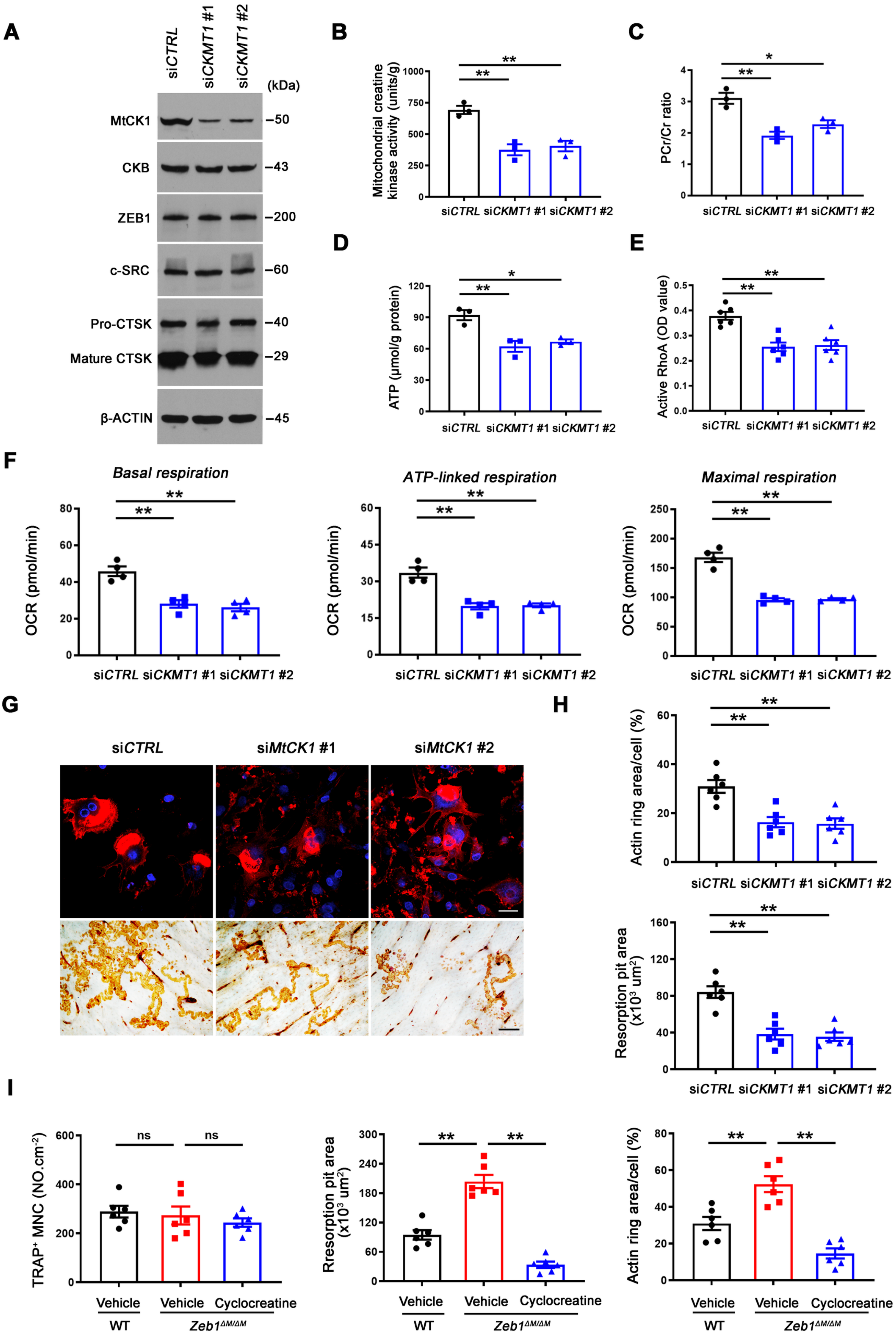

EMBJ_2565_EMBOJ2022111148R2_FigEV5.tif